Improving Precipitation Estimates from Dual-Wavelength Radars

Marco A. Perez

Department of Atmospheric and Oceanic Sciences

McGill University, Montreal, Quebec

A thesis submitted to McGill University in partial fulfillment of the requirements

for the degree of Master of Science

February 2003

National Library
of Canada

Acquisitions and
Bibliographic Services

395 Wellington Street
Ottawa ON K1A 0N4
Canada

Bibliothèque nationale
du Canada

Acquisisitons et
services bibliographiques

395, rue Wellington
Ottawa ON K1A 0N4
Canada

Your file Votre référence
ISBN: 0-612-88281-0
Our file Notre référence
ISBN: 0-612-88281-0

Canada

Abstract

Dual-wavelength radars can, in principle, provide extra information to help in the estimation of precipitation. One method would be to use the differential attenuation measured between the two frequencies of the radar as an indication of the rain rate. Microwave attenuation is widely regarded as a good estimator of the intensity of precipitation. The theory of microwave attenuation is presented, as well as an estimation of the error sources involved in the measurement of attenuation with dual-wavelength radars. Two long-time datasets of disdrometer data are used to test the feasibility of tuning the radar $Z-R$ relationship by measuring the relation between reflectivity and X-band attenuation. As an interesting fact, a surprising proportionality between these two variables is found for higher intensities of precipitation ($Z > 40dBZ$). This finding limits the capabilities of dual-wavelength radars to use attenuation as a second parameter, since at higher reflectivities X-band attenuation is almost equivalent to reflectivity. This also has strong implications for any other method involving X-band attenuation as a means to improve upon reflectivity-only estimation of rainfall rate. Finally, a method is presented that makes use of radar-measured attenuation to externally calibrate a dual-wavelength radar system. Actual radar measurements are presented and compared to disdrometer data.

Résumé

L'information additionnelle fournie par un radar à deux longueurs d'onde pourrait en principe aider l'estimation de précipitation par mesure radar. Une méthode serait l'utilisation de l'atténuation différentielle entre ses deux fréquences comme indication de l'intensité de précipitation. L'atténuation des micro-ondes est communément considérée comme un bon moyen d'estimer l'intensité de précipitation. La théorie concernant l'atténuation des micro-ondes est présentée, ainsi qu'une estimation des sources d'erreur affectant la mesure de l'atténuation avec un radar à deux longueurs d'onde. Deux séries de donnés de disdromètre sont utilisées pour évaluer la faisabilité d'ajuster la relation $Z-R$ en mesurant la relation entre la réflectivité et l'atténuation dans la bande X. Cependant, pour des valeurs plus intenses de précipitation ($Z > 40dBZ$) nous trouvons une surprenante proportionnalité entre ces deux variables. Ce fait limite l'utilisation de l'atténuation dans la bande X comme un second paramètre, car pour les grandes intensités, cette atténuation est presque proportionnelle à la réflectivité. Il a aussi des implications importantes pour toute autre méthode qui voudrait utiliser l'atténuation dans la bande X pour améliorer les estimations de précipitation à partir de la réflectivité. Finalement, nous présentons une méthode pour la calibration du radar en utilisant la relation entre l'atténuation mesurée et la réflectivité. Des donnés radar réelles sont comparées à celles du disdromètre.

Acknowledgements

The work presented in this thesis would not have been possible without the help and support of a large number of colleagues and friends. I would like to thank my supervisor Prof. Isztar Zawadzki, first for accepting me in McGill as a part of his radar group, then for providing the pressure and persistence that make us learn and progress. I would also like to express my gratitude to the staff of the Department of Atmospheric and Oceanic Sciences and the Marshall Radar Observatory for offering a very pleasant work environment. I am particularly grateful to GyuWon Lee and Edwin Campos for their valuable comments and help providing part of the data used in this thesis and to Dr. Barry Turner for proofreading the manuscript.

Quiero también expresar mi gratitud al Dr. Orlando Rodríguez del Centro Meteorológico de Camagüey por introducirme al mundo de los radares meteorológicos y por la escuela que él constituye.

Una mención muy especial merece el apoyo brindado por mis padres y esposa, así como la inspiración y el compromiso que representa mi hijo. El cariño reduce la distancia que nos separa.

¡Muchas gracias!

Contents

List of figures

List of tables

1 Introduction

1.1 Motivation

The MRL-5 radar in Camagüey, Cuba was upgraded in 1997 from its previous manual operation mode to a fully computer-controlled system [Perez et al., 1999]. This modification made possible the use of the radar for quantitative precipitation estimation. The rest of the radars in the Cuban network are going through a similar revamping process [Rodriguez et al., 2001] within a national radar modernization program. The radar at Pico San Juan, Cienfuegos was updated in the summer of 2000 and the one in Casablanca, Havana followed in the spring of 2001.

Four of the seven operational weather radars in Cuba are Russian-built dual-wavelength MRL-5 radars (see Appendix D) comprising S- and X-band frequencies. These include the radars at Camagüey, Pico San Juan and Casablanca whose data output is available in digital format. Another MRL-5 radar at Pilón is still operated manually. The rest of the Cuban radars are RC-32B by Mitsubishi, Japan with S-band capabilities only.

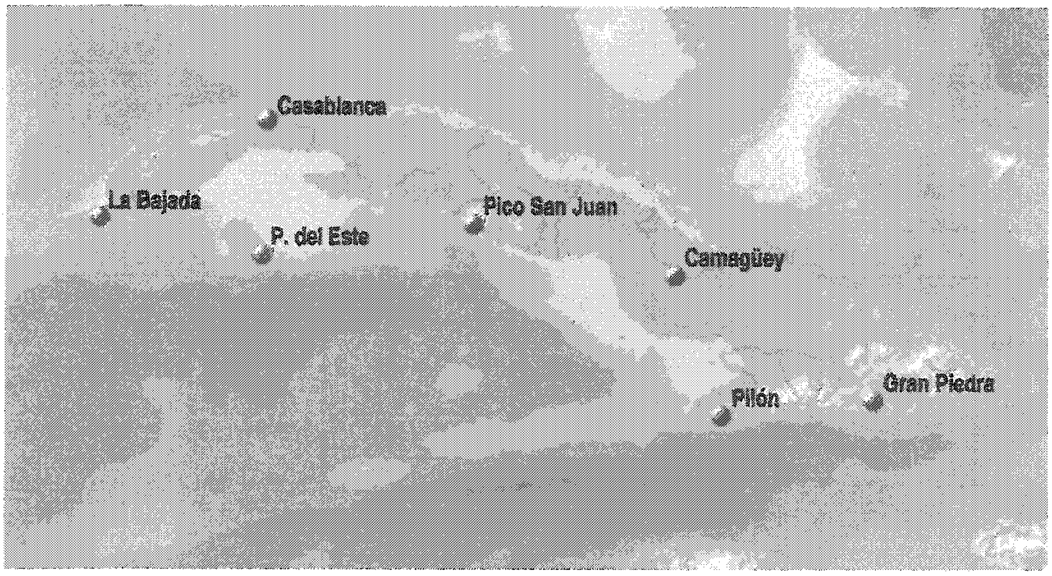

Fig. 1-1: Weather radars in Cuba.

Traditionally radars in Cuba have been used to track hurricanes, cold fronts, and severe storms in order to provide short-term warning to affected areas. However, starting with the joint Cuban-Soviet experiments on precipitation enhancement [Koloskov et al., 1995] the demand for accurate quantitative surface rainfall accumulations has been increasing.

Despite the fact that the X-band channel on MRL-5 radars is very powerful by world standards (compare MRL-5 characteristics in Appendix D with MRO characteristics in Appendix C), in Cuba it has been under-utilized for many years. This is partially due to higher operational costs compared to the S-band channel, but mainly because of the attenuation introduced by heavy rain at the X-band frequencies [Hitschfeld and Bordan, 1953]. As a result, the X-band channel has been mostly abandoned and only S-band reflectivity is used to estimate precipitation.

The main objective of this thesis is to explore whether attenuation measured with dual-wavelength radars could be used as a second parameter to refine the estimation of precipitation rates, making it in principle more accurate than employing S-band reflectivity alone.

Authors as early as Austin (1947) have proposed the use of measured attenuation to gain insight into precipitation. Particularly, Atlas and Ulbrich (1974) and Atlas and Ulbrich (1977) describe relationships for estimating the rainfall rate directly from attenuation at X-band frequencies.

More recently, interest in attenuation methods for estimating precipitation has been renewed with the launch of the Tropical Rainfall Measurement Mission (TRMM) [Kumerow et al., 1998] and plans for the Global Precipitation Measurement (GPM) [Kozu and Nakamura, 1991; Kumerow et al., 2000].

1.2 Precipitation estimation with radar

The estimation of precipitation is one of the most important tasks of radar meteorology, not only because of the significance of precipitation in meteorology but also for the large influence that an accurate measurement of precipitation can have on the economy.

In Camagüey, during the cropping season, the Ministry of Sugar-cane Agriculture uses hourly accumulations of rainfall to distribute its heavy cutting machinery to regions where it can safely operate. Also, the provincial Department of Hydro-economy manages the level of water reservoirs in the territory partially by using radar data. The goal is to prevent floods while yet storing the maximum possible capacity of water.

Conventionally, precipitation has been estimated by means of rain gauge networks, which can only measure point accumulations. On the other hand, radars can provide almost instantaneous measurements over very large areas.

However, radars cannot directly measure precipitation as rain gauges do. They measure the *reflectivity* of atmospheric targets. The target, in the case of rain, are raindrops falling through the atmosphere. Raindrops can be modeled as somewhat deformed water spheres [Pruppacher and Beard, 1970], with the most important parameters being their size and concentration.

The usual choice to categorize the size of a deformed raindrop is the diameter of an equivalent spherical drop with the same volume. This dimension is called the equivalent diameter (D_e or simply D), and it is usually expressed in millimeters. The concentration is the number of drops per unit volume and per unit size interval. With volume in cubic meters and size in millimeters it has units of $mm^{-1}m^{-3}$.

When the size of raindrops is small compared to the radar wavelength [Battan, 1961], the reflectivity of a volume of rain is proportional to the summation of the sixth power of the diameters of its contained particles ($Z \propto \sum D^6$). On the other hand, the rainfall rate has been found [Atlas and Ulbrich, 1977] to be approximately proportional to the 3.67th power of the particle diameters ($R \propto \sum D^{3.67}$).

The classical method for rainfall estimation with radar consists on establishing an empirical relationship between radar-perceived reflectivity and rainfall rate. The usual assumption is a power law in the form $Z = aR^b$. The reflectivity measured by the radar for every coverage volume is converted to a rainfall rate value using the $Z-R$ relationship and it is then integrated over time to produce an estimate of rainfall accumulation.

1.3 Z-R relationships

The choice of the $Z-R$ relationship is crucial for correctly estimating precipitation using the method described above. Therefore, a lot of effort has been put into finding the best $Z-R$ relationship for a particular climate, season, or type of precipitation as a means of reducing the errors in the conversion from reflectivity to rain rate.

Marshall and Palmer (1948) proposed $Z = 200R^{1.6}$, a relationship that has been widely used for stratiform precipitation. However, many other $Z-R$ relations have been proposed in the literature [e.g. Battan, 1973; Stout and Mueller, 1968]. In Cuba, it is customary to use a relationship obtained by Woodley et al. (1975) for convective rain in Florida*, $Z = 300R^{1.4}$.

---

* This is also the default $Z-R$ relationship for NexRad WSR-88D radars [Fulton et al., 1998].

Campos and Zawadzki (1999) argue that instrumental uncertainties in determining the coefficients of average $Z-R$ relationships are of the same order of magnitude as the difference between the coefficients of previously proposed relationships. They also find that the choice of integration parameters (i.e. averaging time, minimization method) even if for the same instrument and dataset would yield a similar difference in the coefficients.

The parameters of the $Z-R$ relationship depend on the shape of the drop size distribution of the precipitation (DSD). Lee and Zawadzki (2002) find a good correlation between the microphysics of the process above the melting layer and the shape of the resulting drop size distribution at ground. This could provide some evidence for the selection of a $Z-R$ relationship according to microphysics or at least justify the existence of locally stable $Z-R$ relations.

1.4 Multi-parameter measurements

Conventional radars measure only reflectivity (Z). However, polarimetric radars add at least differential reflectivity (Z_{DR}) as a second parameter and, if phase information is available, also differential phase shift (Φ_{DP}) and its spatial derivative, the specific differential phase shift (K_{DP}). Radars with two wavelengths or more can be used to measure specific attenuation (K) or differential attenuation depending on the choice of frequencies.

All these measurable parameters can be related to moments of the DSD. However, none is equivalent to the most wanted parameter of rain rate (R). Two lines of research have been followed in order to enable radars to better estimate R. The first is searching for a radar measurable with a kernel (moment of the DSD) as close as possible to that of rain rate. The second technique is to assume a model drop size distribution and estimate its parameters from multi-parameter radar measurements, then integrate the DSD to get the rain rate. Both of these two methods have drawbacks that have prevented them from becoming operational.

First, none of the multi-parameter variables with kernels close to rain rate can be measured with as good a spatial resolution as reflectivity. This is because the best candidates K and K_{DP} are both spatial derivatives of a measured quantity. That is, what radars measure is the integral of K, namely total attenuation, or the integral of K_{DP}, which is Φ_{DP}. Then, K or K_{DP} have to be calculated as the spatial derivative of the measured quantity, therefore amplifying the noise in the initial measurements.

The second method introduces at least two additional error sources: that of measuring the extra parameter and that of assuming an *a priori* DSD model (which introduces an error as well). Only if the combined error is smaller than the error caused by estimating R using Z alone would the method be useful.

The result is that up to the present multi-parameter measurements have not been successfully used to improve precipitation estimates in operational radars.

Doviak (1983) presents a comprehensive discussion about various rain estimation methods including directly computing the rainfall rate from other variables as well as using multi-parameter measurements. Testud et al. (2000) elaborate in the use of multi-parameter radar measurements in the context of polarimetric radars.

1.5 Dual-wavelength radar

Dual-wavelength radars sense the atmosphere with two different frequencies. The most frequent design is to employ a non-attenuating wavelength coupled with another wavelength for which attenuation is significant. This is the case for dual-wavelength radars operating simultaneously within the S-band and the X-band.

Fig. 1-3 shows an example of an actual reflectivity field as observed by a dual-wavelength radar. The image on the top shows the reflectivity field as measured with the S-band channel while the image in the bottom corresponds to the same reflectivity field as observed with the X-band. In both images the radar station is located at the center of the image.

The attenuation experienced by the shorter wavelength is evident in the area behind (from the radar point of view) the frontal line of high reflectivities that runs approximately from north-west to south-east. In some areas the attenuation is so strong that the X-band signal is completely lost. Attenuation introduced by intense precipitation cells appears as a wedge-like pattern of lower X-band reflectivities spreading behind the cell.

Eccles and Atlas (1973) proposed the use of dual-wavelength radars to detect hail. The rationale is that large hailstones behave as non-Rayleigh scatterers at the shorter wavelength but still can be regarded as Rayleigh scatterers at the longer wavelength. Therefore, if rain attenuation is corrected using the non-attenuated reflectivity, the ratio of the two reflectivities can be used as an indication of the presence of hail. However, hail is not a big concern in Cuba and hailstones never reach the size that would make them detectable to a dual-wavelength radar.

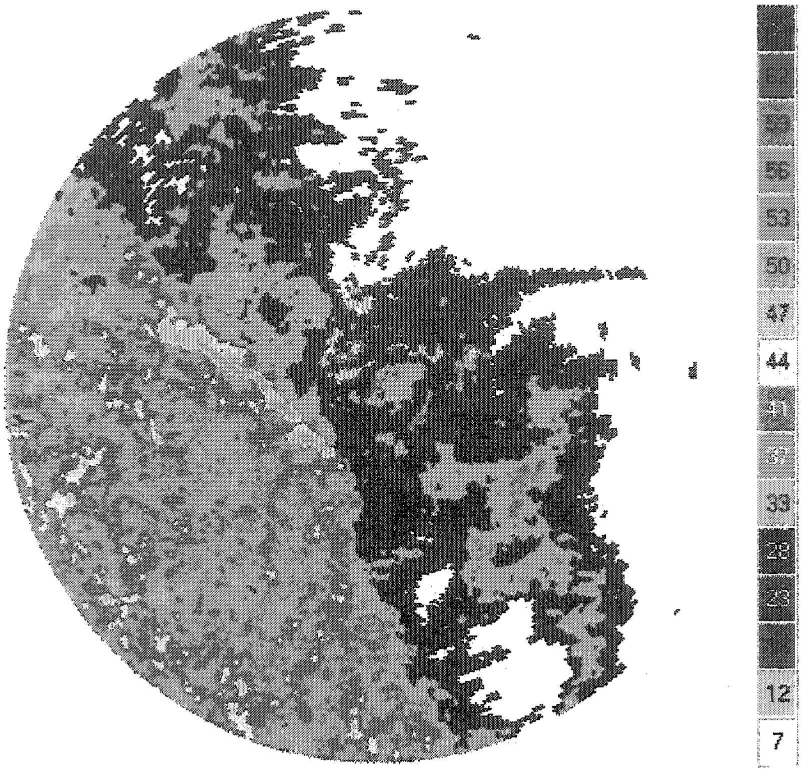

Fig. 1-2: Radar reflectivity field measured with S-band.

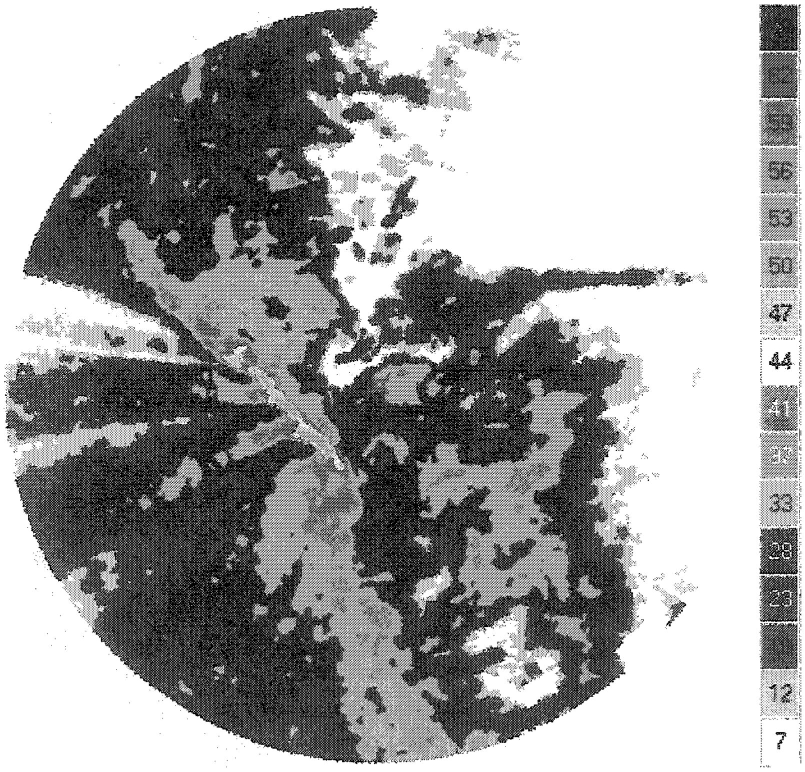

Fig. 1-3: Same reflectivity field measured with X-band.

More important to this work is the paper presented by Eccles (1979) that demonstrates the feasibility of measuring rain attenuation with dual-wavelength radars. His work also presents encouraging improvements in rainfall accumulations derived directly from attenuation.

In the context of MRL-5 radars, Melnichuk and Pavlyukov (2001) propose a minimization algorithm for operationally adjusting $Z-R$ relationship. These authors try to match the measured X-band reflectivity field to that measured with the S-band by correcting the X-band attenuation with an algorithm similar to Hitschfeld and Bordan (1953). They change the coefficients of the $Z-R$ relationship to obtain the best possible match between the two fields. This approach has the disadvantage that it does not account for possible radome attenuation, which can be particularly severe for the X-band. Also, neither polarization nor Mie scattering effects are included in the algorithm.

1.6 Objective and outline

The main objective of this thesis is to explore the possibility of using information provided by rain attenuation to improve the estimation of rainfall accumulations with dual-wavelength radars. We also want to accomplish this goal with existing technology and without sacrificing temporal or spatial resolution.

A secondary goal is to document the main sources of error involved in measuring attenuation with a dual-wavelength radar and to develop procedures for extracting attenuation information from dual-wavelength data. A less important aspiration of the thesis is to condense the theory and equations involved in attenuation and dual-wavelength radars so the manuscript can function as a reference tool for future work on the Cuban MRL-5 radars.

The thesis has been divided in seven chapters, including this introduction (Chapter 1), and four appendixes. Chapter 2 deals with the equations and theory involved in the attenuation of electromagnetic radiation. An algorithm for tuning radar $Z-R$ relationships using attenuation is proposed. A second algorithm for correcting radar calibration errors is also studied. Chapter 3 presents a simulation using disdrometer data intended to evaluate the viability and possible performance of the proposed algorithms. Chapter 4 discusses the errors inherent in attenuation measurements with dual-wavelength radars. Particular emphasis is put on a limited dataset acquired with the dual-wavelength radar at the Marshall Radar Observatory of McGill University. The applicability of the proposed algorithm to dual-wavelength data and its implications is discussed in Chapter 5. Meanwhile, the radar calibration results obtained from the MRO dataset are presented in Chapter 6. The conclusions of the thesis are presented in Chapter 7. The four appendixes describe the characteristics of the instruments and radars used in the thesis.

2 Attenuation of electromagnetic waves

2.1 Atmospheric attenuation

While traveling through a material medium, electromagnetic radiation experiences attenuation due to scattering and absorption. The loss in radiation intensity introduced along a path segment can be expressed as:

$$dI = -\frac{1}{dV}\left(\sum_{i=1}^{N}\sigma_{t\,i}\right) I dS \qquad [W] \qquad (2\text{-}1)$$

In this equation, it is assumed that the displacement dS is small and the intensity I does not change much along the path segment. The total attenuation cross-section σ_t (also referred to as the extinction cross-section [Atlas, 1953]) is the sum of the scattering cross-section σ_s and the absorption cross-section σ_a of every particle within the volume dV.

If the attenuation coefficient is defined as:

$$k = -\frac{1}{dV}\left(\sum_{i=1}^{N}\sigma_{t\,i}\right) = \int_0^{\infty} N(D)\sigma_t(D)dD \qquad [m^{-1}] \qquad (2\text{-}2)$$

The attenuated intensity of the electromagnetic signal at range r_0 is then:

$$I_A(r_0) = I(r_0)e^{-\int_0^{r_0} kdr} \qquad [W] \qquad (2\text{-}3)$$

In the case of radar, electromagnetic waves traverse the same medium twice. For this reason, a two-way attenuation factor is commonly used. The attenuated radar reflectivity factor is then:

$$Z_A(r_0) = Z(r_0) - \int_0^{r_0} Kdr \qquad [dBZ] \qquad (2\text{-}4)$$

With $K = 2\times 10\log e \times 10^3 k \qquad [dBkm^{-1}] \qquad (2\text{-}5)$

2.1.1 Gaseous attenuation

Only oxygen and water vapor are important when considering attenuation introduced by atmospheric gases at radar wavelengths [Battan, 1973]. The attenuation introduced by atmospheric oxygen is, according to Bean and Dutton (1968), approximately the same for S-band and X-band wavelengths. The attenuation introduced by water vapor at these frequencies is different but smaller [Van Vleck, 1947b]. The following are approximate values for the attenuation coefficients of oxygen and water vapor at 20°C [Sauvageot, 1983]. Sea-level pressure is used in the case of oxygen attenuation:

$$K_{O_2}^{S} \approx K_{O_2}^{X} \approx 2\times 8\times 10^{-3} \qquad [dBkm^{-1}] \qquad (2\text{-}6)$$

$$K_{H_2O}^{S}(P,W) \approx 2\times 7\times 10^{-5}\,PW \qquad [dBkm^{-1}] \qquad (2\text{-}7)$$

$$K_{H_2O}^{X}(P,W) \approx 2\times 7\times 10^{-4}\,PW \qquad [dBkm^{-1}] \qquad (2\text{-}8)$$

where P is the pressure in atmospheres and W is the water vapor content in gm^{-3}.

With the accuracy of current weather radars in the order of $1\,dB$, the attenuation introduced by atmospheric gases at S-band and X-band frequencies can be safely neglected for distances up to about $100\,km$.

2.1.2 Cloud attenuation

For cloud droplets, the Rayleigh approximation is always valid at radar wavelengths. The absorption and scattering cross-sections can then be expressed as:

$$\sigma_a = \frac{\pi^2}{\lambda}\,\mathrm{Im}\{-K_W\}D^3 \qquad (2\text{-}9)$$

$$\sigma_s = \frac{2}{3}\frac{\pi^6}{\lambda^4}|K_W|^2 D^6 \qquad (2\text{-}10)$$

Absorption dominates over scattering for wavelengths greater than $0.5\,cm$. As a result the attenuation cross-section of cloud particles may be written as:

$$\sigma_{t\,cloud} \approx \sigma_a \propto D^3 \qquad (2\text{-}11)$$

Then, the attenuation factor for a cloud volume is proportional to the cloud liquid water content (LWC):

$$K_{cloud} \propto \sum D^3 \propto LWC \qquad (2\text{-}12)$$

For frequencies below the X-band, cloud attenuation can be safely neglected. Nevertheless, for X-band frequencies and above, it can be significant. For T =20°C, Gunn and East (1954) give:

$$K_{cloud}^{X}(LWC) \approx 2 \times 0.0483 LWC \qquad [dBkm^{-1},\ LWC \text{ in } gm^{-3}] \qquad (2\text{-}13)$$

The coefficient in the equation above depends on temperature. In general, for the X-band cloud attenuation decreases with increasing temperature.

In the present work attenuation is measured along paths only a few kilometers long. Therefore, cloud and gaseous attenuation are neglected. Instead we only consider attenuation from rain and its relation to rainfall rate and radar reflectivity.

2.1.3 Rain attenuation

Raindrops have greater dimensions that cloud droplets. For this reason, the Rayleigh approximations for attenuation used before cannot be applied to rain. Instead, Atlas and Ulbrich (1974) propose a power-law approximation for the attenuation cross-section of raindrops as:

$$\sigma_t(D) = CD^n \qquad [cm^2; D \text{ in } cm] \qquad (2\text{-}14)$$

In addition, they note the dependence of the constants C and n on wavelength and temperature (Fig. 2-1 and Fig. 2-2).

For radar wavelengths, the scattering cross-section of raindrops cannot be neglected. Therefore the exponent n in the power-law equation is generally greater than three. The attenuation coefficient of rain (K_{rain}) cannot simply be related to liquid water content as for cloud.

Fig. 2-3 and Fig. 2-4 show a comparison between Mie-calculated extinction cross-sections, those calculated using the power-law proposed above and the Rayleigh approximations. For Rayleigh results, the absorption cross-section only and the absorption cross-section plus scattering cross-section are shown. These simpler, alternative, solutions provide accurate values only for a limited range of drop sizes. Note that the Mie curve in Fig. 2-4 is not a straight line. Therefore, the Mie equations must always be used for precise results [Delrieu et al., 1991].

It is convenient to express rain attenuation as a function of the precipitation rate. This depends on the liquid water content and the fall velocity of drops, the latter in turn depending on the size of the drops [Bean and Dutton, 1968].

Atlas and Ulbrich (1977) give at T =10°C:

$$K_{rain}^{X} = 0.021 R^{1.16} \qquad [dBkm^{-1}; R \text{ in } mmh^{-1}] \qquad (2\text{-}15)$$

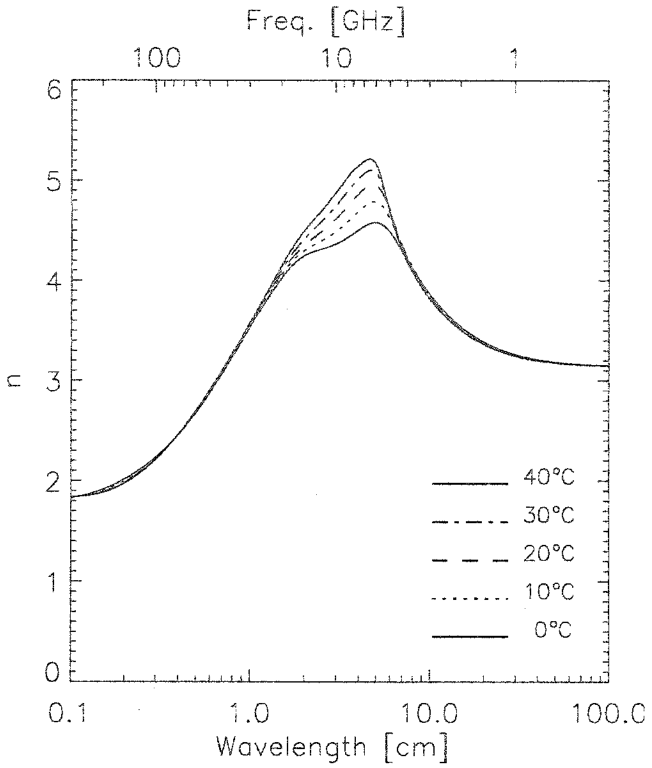

Fig. 2-1 Exponent n of the power-law for attenuation cross-section.

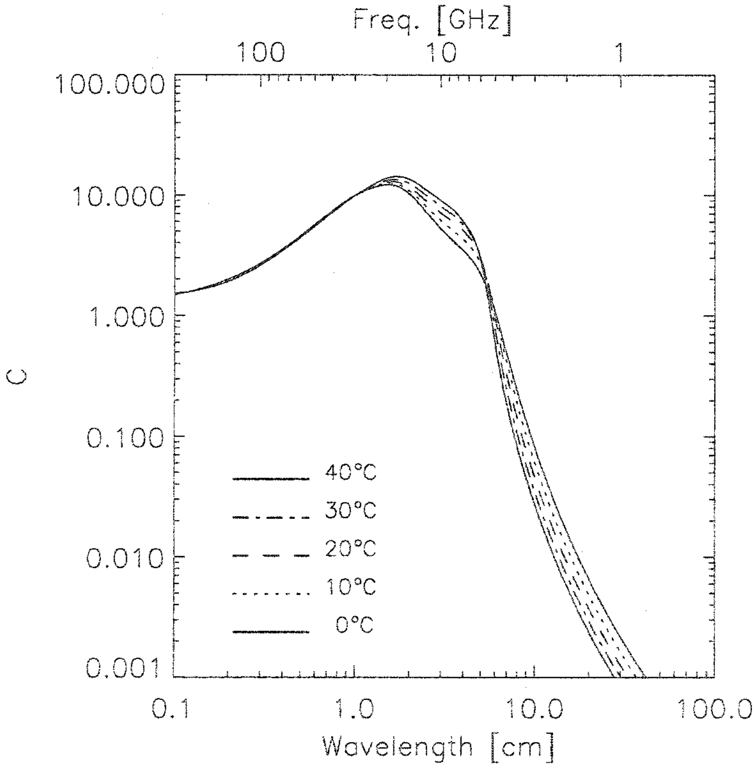

Fig. 2-2 Coefficient C of the power-law for attenuation cross-section.

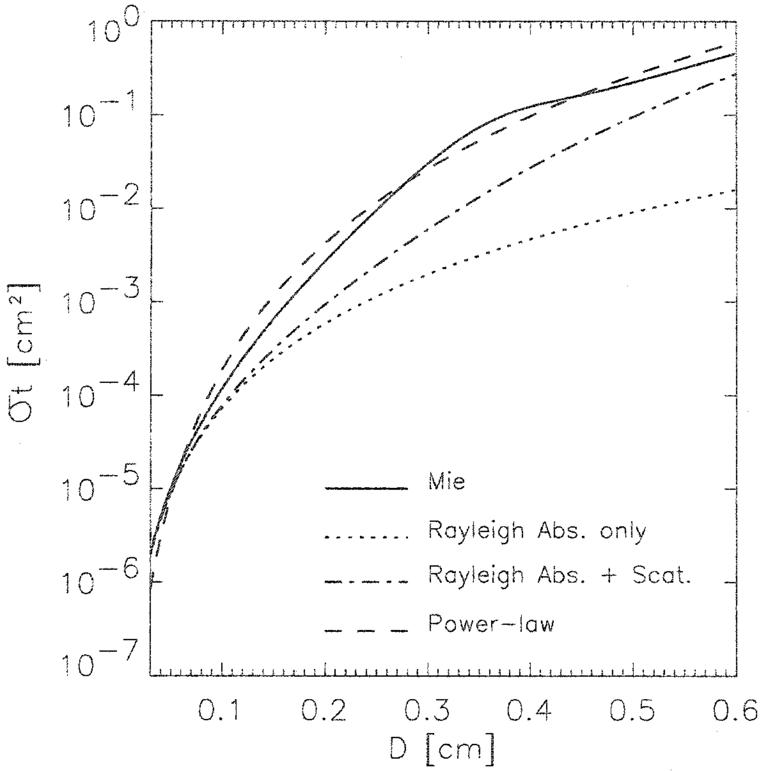

Fig. 2-3 Total attenuation cross-section of raindrops for the X-band at T=15°C.

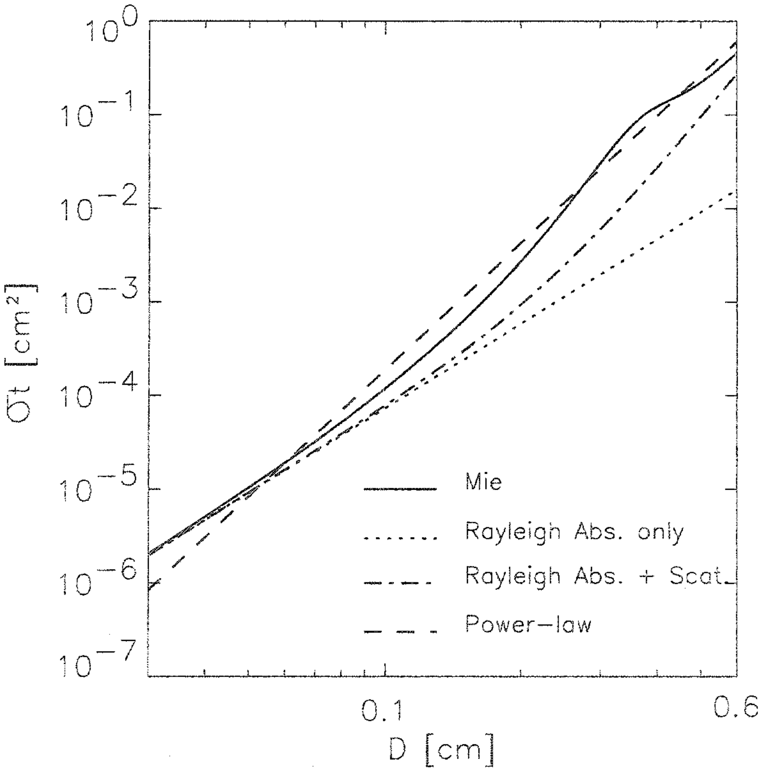

Fig. 2-4 Same as Fig. 2-3 but diameter is in logarithmic units.

2.2 Wet radome attenuation

Radomes used to protect radar antennas introduce a small attenuation by themselves. However, when precipitation occurs on top of a radar station a thin water film develops on the surface of the radome that can increase attenuation many times. Short wavelengths are particularly sensitive to this situation. This is an important point that has not always been accounted for in the literature, e.g. Melnichuk and Pavlyukov (2001).

Measuring and correcting wet radome attenuation is particularly challenging because of the many factors affecting it, such as: precipitation intensity, wind speed, temperature, radome geometry and material, etc. However, this is a problem that cannot be avoided in an operational procedure.

In our approach we will be using dual-wavelength radars to measure average attenuations along radial paths. In this setup we match the reflectivity measured with the attenuated wavelength to that of the non-attenuated wavelength at the beginning of the segment, effectively removing short-wave attenuation introduced prior to that point. Then we compute the total segment attenuation as the difference between the two reflectivities at the end of the trajectory.

2.3 Ground attenuation and blocking

Ground objects can partially or even totally intercept the electromagnetic radiation of the radar. This reduces the power of the signal that travels to and from a target and hence can be interpreted as an attenuation effect.

Topography blocking depends strongly on the location of the radar station. It can be particularly severe for radars operating in mountainous regions. Besides this, the intensity of clutter depends on radar wavelength, antenna beam-width, side-lobes, and maybe even polarization.

In our measurements of attenuation we do not correct for ground-introduced beam blocking. Instead, we adjust the limits of the radial segments described in the previous section to avoid areas contaminated with ground echoes. If the path limits are set correctly, this method eliminates attenuation sources other than rain. A station clutter mask can be obtained from a digital terrain map or from average radar observations in days with no precipitation.

In addition to ground clutter considerations, the limits of the radial segments used for measuring attenuation should be chosen in a way that the path integrated attenuation is higher than the error of the radar in the estimation of reflectivity (see Section 2.5). Also, we must terminate each segment before it reaches the melting layer region.

2.4 Temperature dependence of rain attenuation

As can be seen from the approximate curves in Fig. 2-1 and Fig. 2-2, the attenuation cross-section of raindrops depends on temperature. This dependence is more pronounced for frequencies around the X-band. It is therefore important to quantify the effect of temperature on the attenuation coefficient of rain and establishing ways of comparing attenuations measured at different temperatures.

Fig. 2-5 shows the behavior of X-band attenuation with increasing temperature and for different values of reflectivity. The plotted values are normalized by the attenuation coefficient at T =15°C. The absolute values of the attenuation coefficient at this temperature are shown in Fig. 2-7. An exponential Marshall-Palmer drop size distribution (see Section 3.1) was employed.

For small rain rates the attenuation factor decreases with increasing temperature, while for higher rain rates it increases with increasing temperature. This peculiar detail seems to be related to a resonance effect in drops larger than $2\,mm$ that occurs for temperatures above 15°C, producing the bulge observed in Fig. 2-6. As the reflectivity increases the concentration of bigger drops also augments and the attenuation trend with temperature is overturned.

Fig. 2-5 gives an idea of the error involved in measuring attenuation if we assume a fixed temperature (e.g. T =15°C). The maximum error is on the order of 20% for the range of temperatures and reflectivities found in precipitation. For reflectivities above $40\,dBZ$ the error is smaller and around 5%.

Reflectivities higher than $40\,dBZ$ contribute most of rain attenuation at X-band. Consequently, we are mostly interested in this range of intensities. In addition, it is difficult to accurately measure the attenuation of precipitation with reflectivity under $40\,dBZ$ because the small value of the attenuation coefficient force the use of long integration paths (see next section). As a result, temperature differences do not appear to be a major source of errors in attenuation measurements.

Nonetheless, if we want to minimize the effect of temperature, and if at least an approximate temperature profile is available, we can apply a simple normalization scheme to measured attenuations in order to bring them all to the same temperature. K shows an almost linear dependence on T for all important values of reflectivity. Therefore, we can linearize the attenuation coefficient around a fixed temperature T_0:

$$K(Z,T) = K(Z,T_0) + \frac{dK}{dT}(Z,T_0) \times (T - T_0) \quad [dBkm^{-1}] \qquad (2\text{-}16)$$

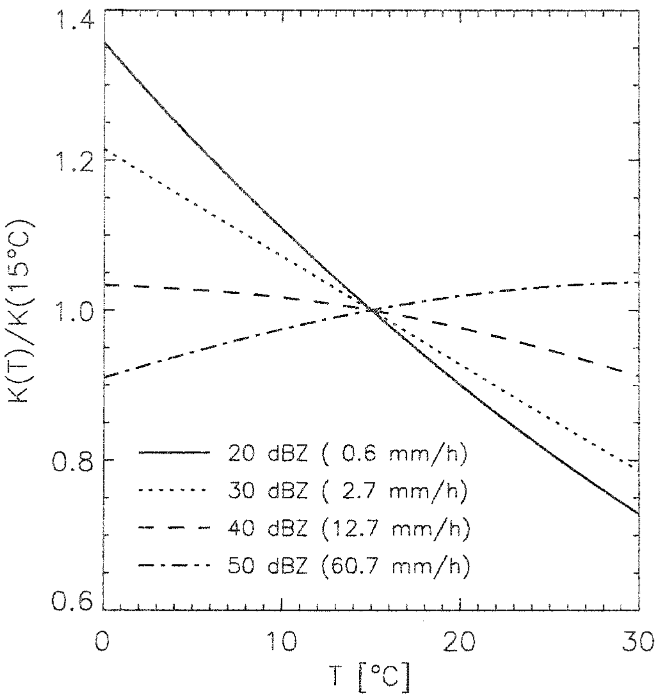

Fig. 2-5 Temperature dependence of the attenuation factor at X-band (MP distribution).

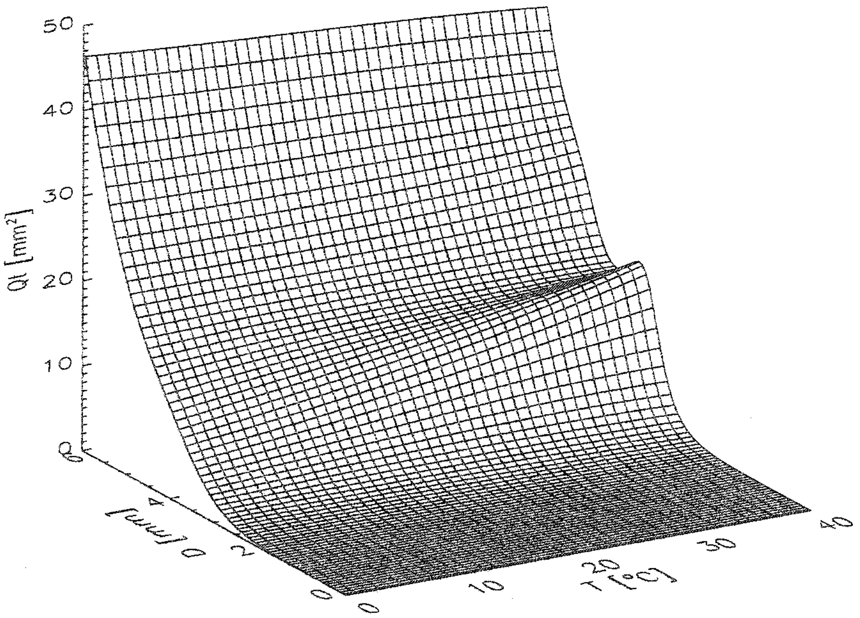

Fig. 2-6: Modeled attenuation cross-section for raindrops at X-band.

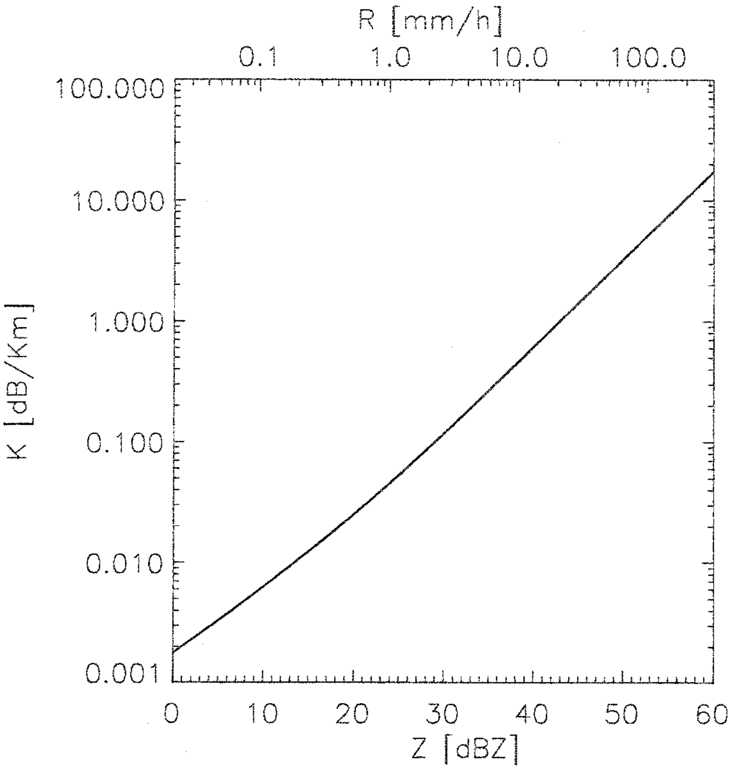

Fig. 2-7: Modeled attenuation factor at X-band, for T=15°C.

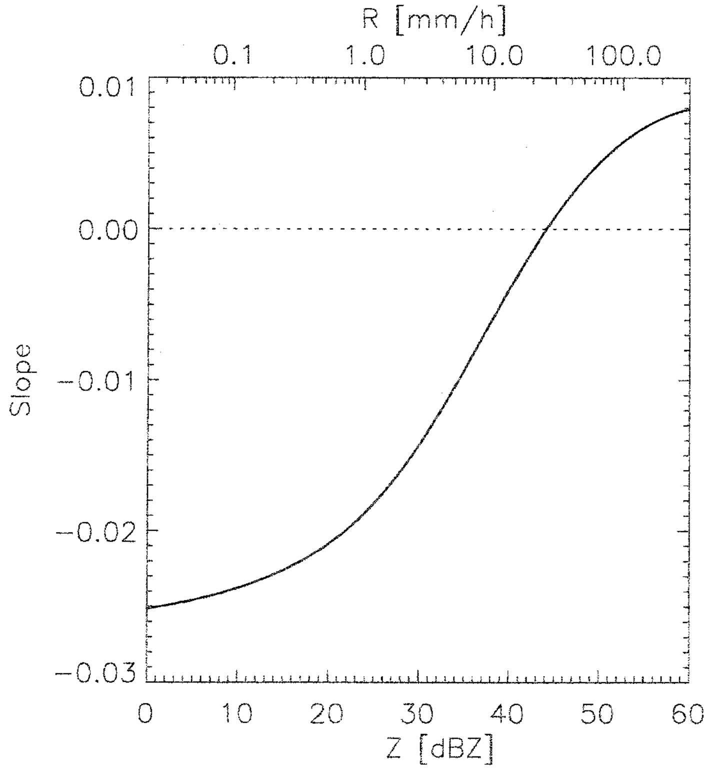

Fig. 2-8: Variation of the temperature dependence of X-band attenuation with reflectivity.

Fig. 2-8 shows the variation of the slope parameter ($\frac{dK}{dT}$) in the equation above for T_0 =15°C. Note the change in the sign of the slope in the region of $Z \cong 44\,dBZ$ ($R \approx 21\,mmh^{-1}$). The values of $K(Z,T_0)$ are those of Fig. 2-7.

2.5 Estimating R directly from K

Using a simple power-law relationship between attenuation cross-section and particle diameter Atlas and Ulbrich (1977) conclude that the attenuation factor of rain and the rainfall rate are linearly related for wavelengths around $1\,cm$ (see Section 2.1.3). These authors also found that for X-band frequencies the relation between R and K is still close to linear. Consequently, if we could correctly measure K, even at the X-band, it would provide a more precise way of measuring precipitation intensity than reflectivity alone.

Dual-wavelength radars can calculate the attenuation coefficient by subtracting the measured attenuated reflectivity from a non-attenuated reflectivity measured with a longer wavelength and dividing this total attenuation by two times the path length.

Since reflectivity is measured with a limited precision we can only expect to measure total path attenuations higher than the accuracy of the reflectivity measurement. The error in the estimation of reflectivity depends on radar characteristics, in particular the number of independent pulses being averaged. This error is usually on the order of $1\,dB$ [Smith, 1964].

Besides, for properly estimating precipitation accumulations, it is necessary to account for rain rates starting as low as $0.1\,mmh^{-1}$ ($Z \approx 10\,dBZ$). However, from Fig. 2-7 we can see that for rain to produce an attenuation higher than $1\,dBkm^{-1}$, reflectivity values in excess of $45\,dBZ$ ($R \approx 25\,mmh^{-1}$) are required. A reflectivity of $20\,dBZ$ ($R \approx 0.5\,mmh^{-1}$) through a path as long as $60\,km$ would only produce a two-way attenuation of $1\,dB$. Thus, for small rain-rates we can only expect to recover averages over large areas.

In conclusion, with current radar setups we cannot measure the full range of attenuation coefficients needed for precipitation estimation without greatly sacrificing resolution. Nevertheless, we can try to use the information we get from path-average attenuation and path-average reflectivity in order to improve the relationship that we use to estimate rain rate from reflectivity. One such use would be locally tuning the $Z-R$ relationship. Another application would be to use X-band attenuation as an external method of calibrating the measurement of reflectivity with the non-attenuating wavelength.

2.6 Proposed algorithm

Dual-wavelength radars can measure rain attenuation as a second parameter of precipitation, although not with the same spatial resolution as reflectivity. We suggest using this second parameter to find localized $Z-R$ relationships that can in turn improve rain rate estimates and accumulations.

If we could tune our $Z-R$ relationships for each particular storm or even regions within the storm, this would improve rainfall estimates over the use of a single, fixed, relationship. For this purpose, a statistical $K-R$ relation is used together with a local $K-Z$ relationship extracted from dual-wavelength reflectivity and attenuation measurements. These two relations are combined to obtain a tuned, or localized, $Z-R$ relationship.

The method is similar to that of Ryzhkov et al. (1997) for polarimetrically tuning $R(Z)$. This work the authors use a fix $K_{DP}-R$ relationship to convert specific differential phase shift values into rain rates and then finding a tuned $R(Z)$ relationship. The rationale of our work is the same, except for using the specific attenuation coefficient K instead of K_{DP} as the proxy variable for precipitation intensity.

Equating the $K-R$ and the $K-Z$ power-law relationships:

$$K = a_{KR} R^{b_{KR}} \tag{2-17}$$

$$K = a_{KZ} Z^{b_{KZ}} \tag{2-18}$$

we get:

$$a_{KZ} Z^{b_{KZ}} = a_{KR} R^{b_{KR}} \tag{2-19}$$

Then, if we solve for a_{ZR} and b_{ZR} in the $Z-R$ power-law relationship $Z = a_{ZR} R^{b_{ZR}}$, we obtain the parameters of our locally tuned $Z-R$ relationship:

$$a_{ZR} = \left(\frac{a_{KR}}{a_{KZ}}\right)^{1/b_{KZ}} \tag{2-20}$$

$$b_{ZR} = \frac{b_{KR}}{b_{KZ}} \tag{2-21}$$

An equivalent method is using the average $K-R$ relationship to convert the measured attenuation coefficients to rain rates, and then getting the tuned $Z-R$ relationship from a direct fit between R and Z.

2.7 Radar calibration

The above algorithm has the interesting peculiarity of being immune to reflectivity calibration errors. For example, suppose that a radar calibration error c_e exists in the measurement of reflectivity. Then, our radar-measured reflectivity is:

$$Z_m = c_e Z \tag{2-22}$$

This calibration error would be included in our locally-fitted (measured) $K-Z$ power-law as:

$$K = a_{KZ}^m Z_m^{b_{KZ}^m} \tag{2-23}$$

Therefore, our tuned $Z-R$ relationship:

$$Z_m = \left(\frac{a_{KR}}{a_{KZ}^m} \right)^{(1/b_{KZ}^m)} R^{(b_{KR}/b_{KZ}^m)} \tag{2-24}$$

or:

$$R = \left(\frac{a_{KZ}^m}{a_{KR}} \right)^{(1/b_{KR})} Z_m^{(b_{KZ}^m/b_{KR})} \tag{2-25}$$

is not affected by the calibration error in reflectivity.

Calibration of weather radars is not an easy task. It is usually assumed to be in the order of 1 dB for reflectivity, but errors of 2-3 dB or even more are not surprising.

The usual radar calibration procedure is to inject the signal from a local microwave generator into the radar receiver and adjusting the receiver gain accordingly. However, the calibration of the whole radar station must also include the antenna gain, radome attenuation and signal loss in the waveguide path from the antenna to the receiver. External calibration is required.

A few methods can be used for external calibration, such as comparing with a known-power external transmitter or using radar returns from targets of known cross-section (e.g. a metal sphere). These methods are costly and are not performed operationally. In practice, radars are calibrated using the average intensity of ground targets, rain gauge accumulations or external disdrometers.

A variation of the tuning algorithm described above could be used for radar calibration, even if our dual-wavelength radar setup does not allow for very precise measurements of attenuation (e.g. non-matched beam-widths).

In this case we need to run the $K-Z$ extraction algorithm for a time long enough for an average (climatological) relationship to appear. Then, we can estimate the radar calibration error as the mean difference between our measured $K-Z$ relationship and the expected relation.

If we consider the measured attenuation factor as error free ($K_m = K$), then a discrepancy between the parameters our measured relationship (a_{KZ}^{m}, b_{KZ}^{m}) and those of the climatological relation (a_{KZ}, b_{KZ}) can be explained either by the existence of a non-average drop size distribution or a calibration error in the measurement of reflectivity. However, if the measured $K-Z$ relation is extracted from a long data series, it is realistic to expect an average DSD. Therefore, a departure of the measured coefficients from our average relation can be interpreted solely as a calibration error in the radar.

Considering a calibration error our measured $K-Z$ relationship is:

$$K = a_{KZ}^{m} c_e^{b_{KZ}^{m}} Z^{b_{KZ}^{m}} \tag{2-26}$$

while the climatological relationship is:

$$K = a_{KZ} Z^{b_{KZ}} \tag{2-27}$$

If we equate these equations and solve for c_e the resulting expression would still contain either Z or K, such as in:

$$c_e = \left(\frac{a_{KZ}}{a_{KZ}^{m}} \right)^{1/b_{KZ}^{m}} Z^{\left(b_{KZ}/b_{KZ}^{m} - 1 \right)} \tag{2-28}$$

That is, we cannot eliminate Z and K simultaneously.

However, a calibration error in reflectivity should not affect the exponent (b_{KZ}^{m}) in our measured relationship. Therefore, in order to eliminate the apparent dependence of c_e on Z (or K), we can set b_{KZ}^{m} equal to b_{KZ}. The coefficient a_{KZ}^{m} has to be re-evaluated to comply with $b_{KZ}^{m} = b_{KZ}$. Our measured $K-Z$ relationship then becomes:

$$K = a_{KZ}^{*} Z_m^{b_{KZ}} \tag{2-29}$$

where a_{KZ}^{*} is the best-fit coefficient for the $K-Z$ relationship with exponent b_{KZ}.

The expression for the calibration error is then:

$$c_e = \left(\frac{a_{KZ}}{a_{KZ}^{*}} \right)^{1/b_{KZ}} \qquad (2\text{-}30)$$

or $$C_e = 10 \log c_e = \frac{10}{b_{KZ}} \log \left(\frac{a_{KZ}}{a_{KZ}^{*}} \right) \qquad (2\text{-}31)$$

in logarithmic units.

The error in the determination of the calibration error can be estimated as:

$$\sigma C_e = \left| \frac{10 \log e}{b_{KZ}} \left(\frac{\sigma a_{KZ}^{*}}{a_{KZ}^{*}} \right) \right| \qquad (2\text{-}32)$$

where σa_{KZ}^{*} is the standard deviation of the coefficient a_{KZ}^{*}.

3 Simulation

3.1 Drop size distribution of precipitation

Rain is composed of water drops of different sizes. Knowing the distribution of the number of drops per volume with size is important because most precipitation parameters can be expressed as moments of this distribution.

A drop size distribution (DSD) is usually described using a drop number concentration function $N(D)$ whose value at $D = D_0$ is the number of drops in the size interval $D_0 - dD/2$ to $D_0 + dD/2$ per unit volume. By convention, $N(D)$ has units of $mm^{-1}m^{-3}$. If $N(D)$ describes the drop size distribution, then:

$$R = 3.6 \times 10^{-3} \frac{\pi}{6} \int_0^\infty N(D) w_t(D) D^3 dD \tag{3-1}$$

$$Z_e = \frac{\lambda^4}{\pi^5 |K_W|^2} \int_0^\infty N(D) \sigma_b(D) dD \approx \int_0^\infty N(D) D^6 dD \tag{3-2}$$

$$K = 2 \times 4.343 \times 10^3 \int_0^\infty N(D) \sigma_t(D) dD \tag{3-3}$$

R, Z_e and K are the rainfall rate, the equivalent reflectivity factor and the two-way attenuation factor respectively. $w_t(D)$ is the terminal fall velocity of raindrops. $\sigma_b(D)$ and $\sigma_t(D)$ are the back-scattering cross-section and the total attenuation cross-section in that order.

If the shape of the DSD is known, relationships between any two moments of the DSD can be derived. This would allow estimation of one moment of the DSD by means of measuring another, which is the classic problem of estimating rainfall rates from radar-measured reflectivity.

Marshall and Palmer (1948), after analyzing filter-paper exposed to precipitation, concluded that the average drop size distribution had an exponential shape that depended on the rainfall rate. They proposed (MP DSD):

$$N(D) = N_0 e^{-\Lambda D} \qquad [mm^{-1} m^{-3}] \qquad (3\text{-}4)$$

$$N_0 = 8 \times 10^3 \qquad [mm^{-1} m^{-3}] \qquad (3\text{-}5)$$

$$\Lambda = 4.1 R^{-0.21} \qquad [mm^{-1}] \qquad (3\text{-}6)$$

Clearly, the coefficients a and b in any power-law $Z-R$ relation would depend on the shape of the drop size distribution. However, in the absence of more localized information we must resort to using a statistical DSD such as the one above; which is an average of many actual DSD and is only valid for long-time and wide-area accumulations.

Zawadzki and Lee (2002) suggest that the shape of the DSD is influenced by the microphysics of the processes above the melting layer. This implies that a particular DSD shape would be locally stable and so would the particular $Z-R$ relationship tied to that distribution.

Moreover, good results have been found [Lee and Zawadzki, 2001; Lee and Zawadzki, 2002] in the estimation of rainfall accumulations with radar through the use of disdrometer-calibrated $Z-R$ relationships as opposed to a fixed $Z-R$ relation.

In Section 2.6, an algorithm was proposed that could take advantage of the measurement of a second integral parameter of the DSD for locally tuning the $Z-R$ relationship. In the following sections, the performance of this algorithm is evaluated using real drop size distributions.

3.2 Disdrometer data

Disdrometers are instruments that classify precipitation particles according to their size. As a result we obtain drop number concentration in designated size intervals that are usually called *channels*.

There are various operating principles that have been used in disdrometers: measuring impact momentum of raindrops in the well known Joss-Waldvogel disdrometer [Joss and Waldvogel, 1967]; optical obscuration of a photo-sensor in the *Optical Spectro-Pluviometer* (OSP) [Hauser et al., 1984] and the *Large Particle Spectrometer* (LPS) [Martinez and Gori, 1999]; and relating the Doppler velocity spectrum of falling raindrops to their size as in the *Precipitation Occurrence Sensor System* (POSS) [Sheppard and Joe, 1993].

Year	*Total days*	*Filtered days*	*Points*
1994	*27*	*4*	*1398*
1997	*20*	*7*	*1108*
1998	*126*	*57*	*13111*
1999	*182*	*45*	*10583*
2000	*18*	*17*	*4169*
2001	*2*	*1*	*876*
Total	***374***	***131***	***31245***

Table 3-1 Summary of McGill POSS dataset.

Year	*Total days*	*Filtered days*	*Points*
2000	*38*	*14*	*3405*
2001	*233*	*94*	*15330*
2002	*85*	*4*	*811*
Total	***356***	***112***	***19546***

Table 3-2 Summary of C. Rica OSP dataset.

3.3 Datasets

Two multi-year datasets were available for this work: a three-year series from a POSS sensor located on the roof of a building in downtown Montreal (Burnside Hall, McGill University) and a two-year series from an OSP sensor in central Costa Rica. Both instruments provide average drop size distributions every one minute. The number of days and individual measurements included in the datasets are shown in Table 3-1 and Table 3-2.

Not all the data were used in this study; in particular, individual days with less than thirty minutes of continuous precipitation were eliminated. Also, in the case of the POSS instrument at McGill University, special care was taken to remove days with solid precipitation, a problem not found in the dataset from Costa Rica.

These disdrometer data series are long enough to encompass the natural variability of drop size distributions. Therefore, the average relationships obtained between the variables derived from the DSD (rainfall rate, reflectivity, attenuation, etc) can be regarded as climatological relations.

3.4 Scattering model

A scattering model was used to evaluate the scattering and attenuation cross-sections of deformed raindrops. The raindrop deformation model employed was that proposed by Pruppacher and Beard (1970). However, partial results obtained using the deformation models suggested by Andsager et al. (1999) have been found to be very similar.

The algorithm used in the scattering model for evaluating the scattering matrix of oblate particles is the T-Matrix algorithm described in Mishchenko (2000). The original source code of the FORTRAN algorithm is available at http://www.giss.nasa.gov/~crmim. The model code was extended to simplify the computation of the back-scattering and attenuation cross-sections.

3.5 Relationships between Z, R, and K

Disdrometer-collected data coupled with a scattering model such as the one mentioned above allow for the examination of average and storm-localized relationships between reflectivity, rain rate, and attenuation factor. These magnitudes were computed as:

$$R = 3.6\times10^{-3}\frac{\pi}{6}\sum_{i=1}^{n} N(D_i)w_t(D_i)D_i^3 dD_i \qquad [mmh^{-1}] \qquad (3\text{-}7)$$

$$Z = \frac{\lambda^4}{\pi^5|K_W|^2}\sum_{i=1}^{n} N(D_i)\sigma_b(D_i)dD_i \qquad [mm^6m^{-3}] \qquad (3\text{-}8)$$

$$K = 2\times4.343\times10^3\sum_{i=1}^{n} N(D_i)\sigma_t(D_i)dD_i \qquad [dBkm^{-1}] \qquad (3\text{-}9)$$

D_i and dD_i are the center diameter and width of each channel of the POSS or OSP disdrometer (see Appendix A and Appendix B). $N(D_i)$ is the number concentration provided by the disdrometer while $\sigma_b(D_i)$ and $\sigma_t(D_i)$ are computed using the scattering model. The values for the raindrop fall velocities ($w_t(D_i)$) were obtained by interpolation of the values provided by Gunn and Kinzer (1949).

Fig. 3-1 through Fig. 3-6 illustrate the scatter and mean relationships between Z, R and K for both McGill and Costa Rica datasets. Reflectivity was computed for S-band with horizontal polarization while specific attenuation was calculated for X-band with vertical polarization. These are the polarizations employed on MRL-5 radars. The mean relationships presented were obtained using a total-fit regression in logarithmic units.

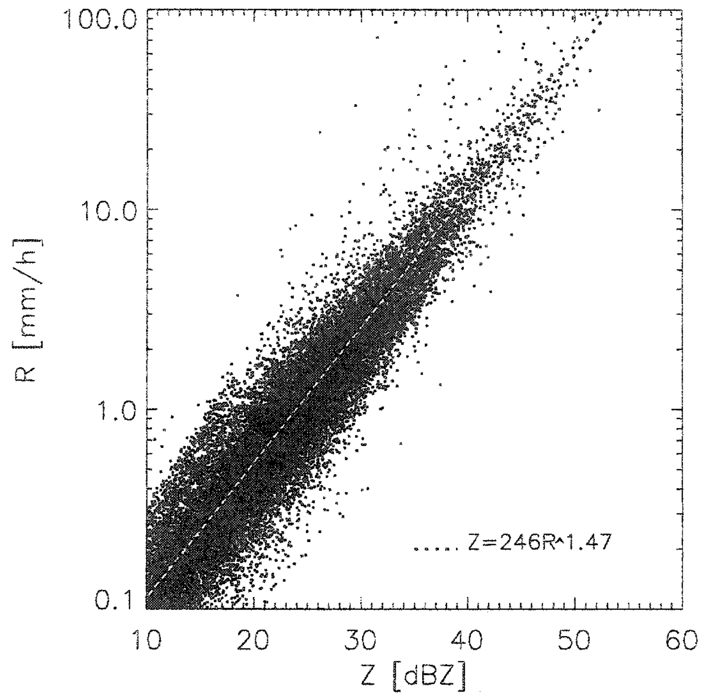

Fig. 3-1: Mean Z-R relationship and scatter, McGill POSS.

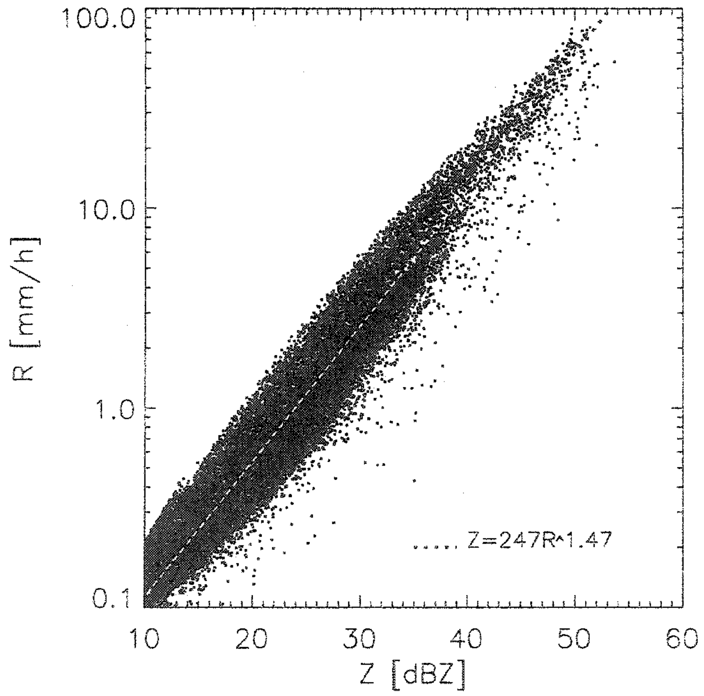

Fig. 3-2: Mean Z-R relationship and scatter, C. Rica OSP.

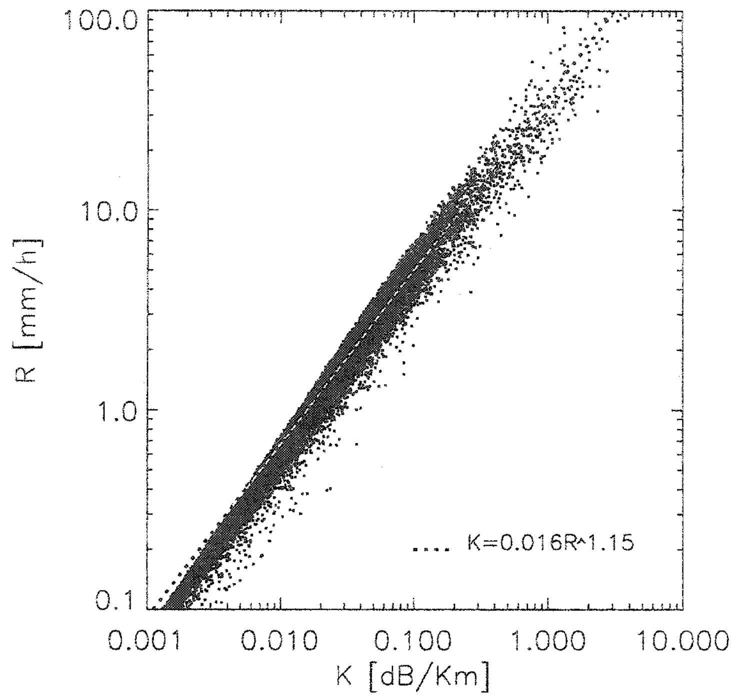

Fig. 3-3: Mean K-R relationship and scatter, McGill POSS.

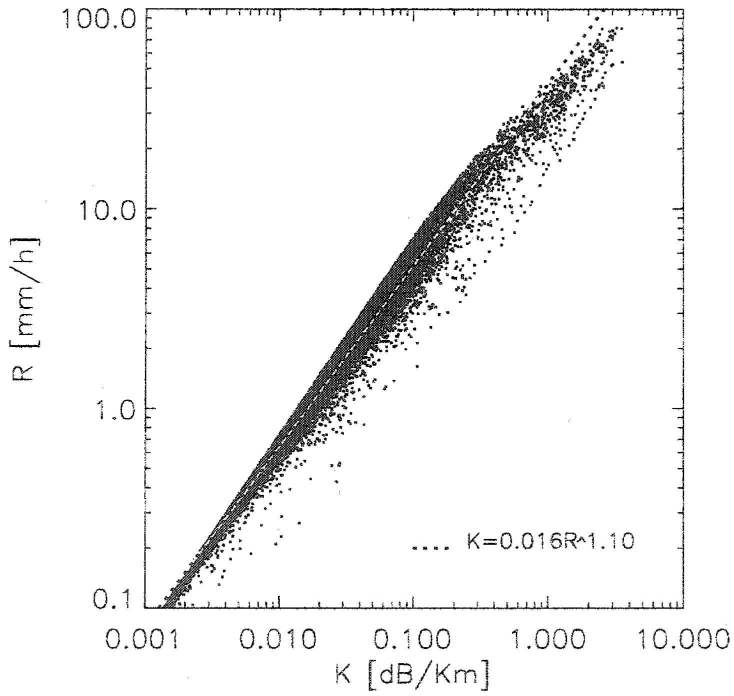

Fig. 3-4: Mean K-R relationship and scatter, C. Rica OSP.

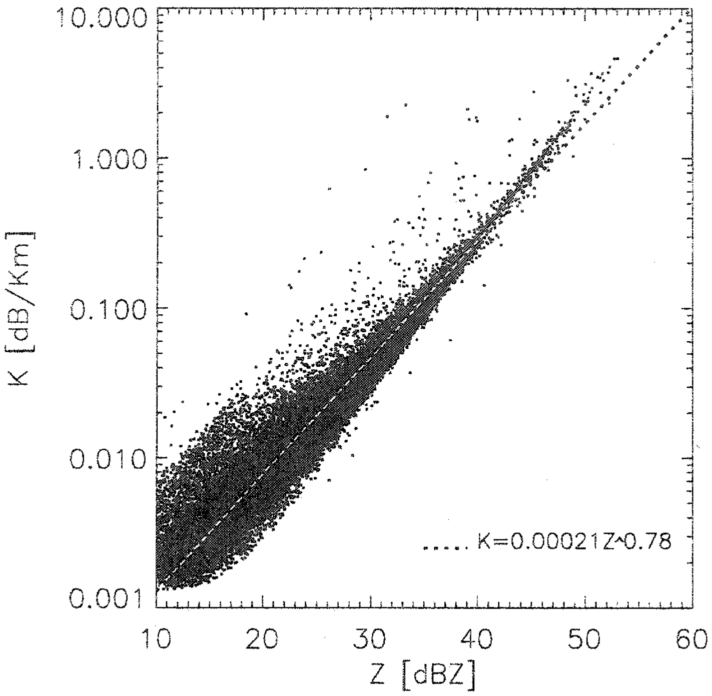

Fig. 3-5: Mean K-Z relationship and scatter, McGill POSS.

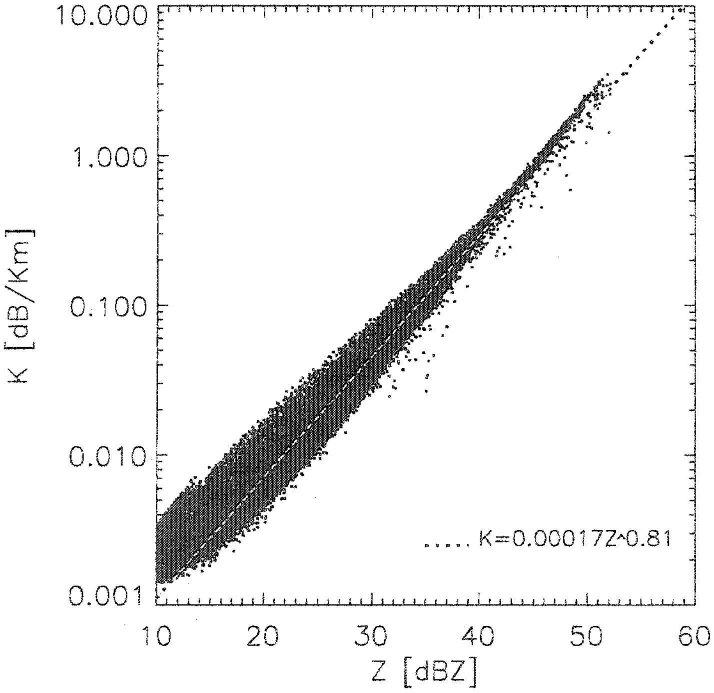

Fig. 3-6: Mean K-Z relationship and scatter, C. Rica OSP.

It should be noted that, as expected by Atlas and Ulbrich (1977), the scatter between K and R is smaller than the scatter between Z and R, a confirmation that the specific attenuation factor is theoretically a better estimator of rain rate than reflectivity. It is also significant that the average $Z-R$ relationships for both datasets are extremely similar, even though the two data series come from very different climates.

The obtained average relationships are in good agreement with the literature [Battan, 1973; Atlas and Ulbrich, 1977; Delrieu et al., 1991]. The only exception is the case of both average $Z-K$ relationships where noticeable deviations from a single power-law relation can be appreciated in the plots of Fig. 3-5 and Fig. 3-6. The causes and implications of this interesting effect are further discussed in Chapter 5.

3.6 Precipitation estimation

In the following sections we present a comparison between different methods of estimating rainfall rates. The following methods are used:

- Single $Z-R$: The climatological power-law relationships between reflectivity and rain rate (Fig. 3-1 and Fig. 3-2) are used to compute the rainfall rate directly from S-band reflectivity.
- Single $K-R$: The climatological power-law relationships between X-band specific attenuation and rain rate (Fig. 3-3 and Fig. 3-4) are used to compute the rainfall rate directly from X-band attenuation.
- Daily $Z-R$: A relationship between reflectivity and rain rate is fitted for each day in the data series. Rain rates are then calculated directly from S-band reflectivity using the individual $Z-R$ relation for the day.
- Daily $K-R$: A relationship between X-band specific attenuation and rain rate is fitted for each day in the data series. Rain rates are calculated from model-calculated attenuation using the individual $K-R$ relation for each day.
- Tuned $Z-R$: The algorithm described in Section 2.6 is used to obtain tuned relationships between reflectivity and rain rate assuming that we know the best $Z-K$ relationship for each day and a climatological $K-R$ relation.

For each method we plot the estimated daily rainfall accumulations against the accumulations calculated from disdrometer data. The accumulations are always calculated in the same manner. The difference between the above methods lies in how each one estimates the rain rate.

3.7 Fixed Z-R vs. daily-fitted Z-R

For evaluating the relative merit of using a fixed $Z-R$ relationship versus the use of daily-tuned relationships, an independent $Z-R$ relation was fitted for each individual day in both of the McGill and Costa Rica disdrometer datasets. A SIF* algorithm was used prior to the regression in order to reduce the scattering.

The resulting daily rainfall accumulations for McGill POSS are plotted in Fig. 3-7 (single $Z-R$) and Fig. 3-8 (daily $Z-R$). Fig. 3-9 and Fig. 3-10 show the corresponding values for Costa Rica OSP. In these four plots, the abscissa correspond to accumulations calculated directly from the integration of disdrometer-measured rain rates, while the ordinates represent the accumulation of rain rates that were estimated from disdrometer reflectivities through $Z-R$ relationships. Each point represents the total rainfall accumulation for each individual day in the data series.

The root mean square error (RMS) and the mean fractional error (MFE) were calculated as:

$$RMS = 100 \times \sqrt{\frac{1}{N}\sum_{i=1}^{N}\left(\frac{A_i^{est.} - A_i^{act.}}{A_i^{act.}}\right)^2} \qquad (3\text{-}10)$$

$$MFE = 100 \times \frac{1}{N}\sum_{i=1}^{N}\sqrt{\left(\frac{A_i^{est.} - A_i^{act.}}{A_i^{act.}}\right)^2} \qquad (3\text{-}11)$$

$A_i^{act.}$ and $A_i^{est.}$ represent the *actual* and *estimated* rainfall accumulation for the i^{th} day.

It should be noted that the fixed $Z-R$ relationships employed in the construction of Fig. 3-7 and Fig. 3-9 were those previously depicted in Fig. 3-1 and Fig. 3-2, which are best-fit relationships for the full McGill and Costa Rica data series respectively. Therefore, the errors in Fig. 3-7 and Fig. 3-9 are the smallest errors achievable with a single $Z-R$ relationship for each dataset. These errors are, of course, smaller than what would be obtained from any other *a priori* $Z-R$ relationship.

A comparison between these figures shows a dramatic reduction in the errors as a consequence of using daily $Z-R$ relationships instead of a single relation. The error estimates plotted in Fig. 3-8 and Fig. 3-10 can be regarded as the maximum attainable accuracy in estimating rainfall accumulations from power-law $Z-R$ relationships for the selected time resolution.

---

* Sequential Intensity Filter: Lee and Zawadzki (2002).

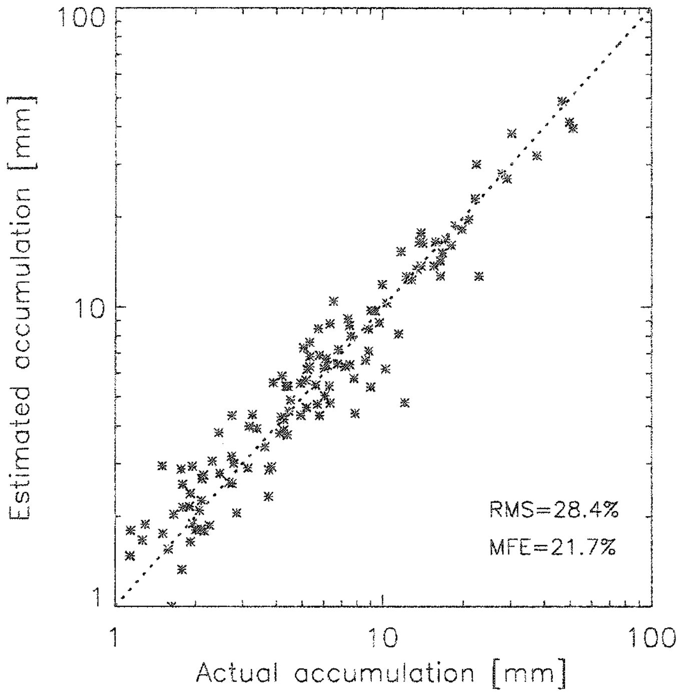

Fig. 3-7: Accumulations from single best Z-R relationship, McGill POSS.

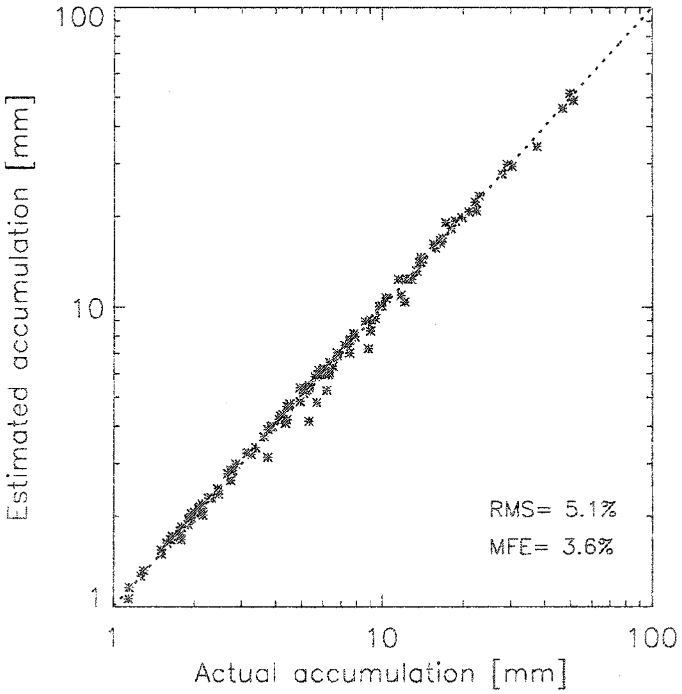

Fig. 3-8: Accumulations from daily-fitted Z-R relationships, McGill POSS.

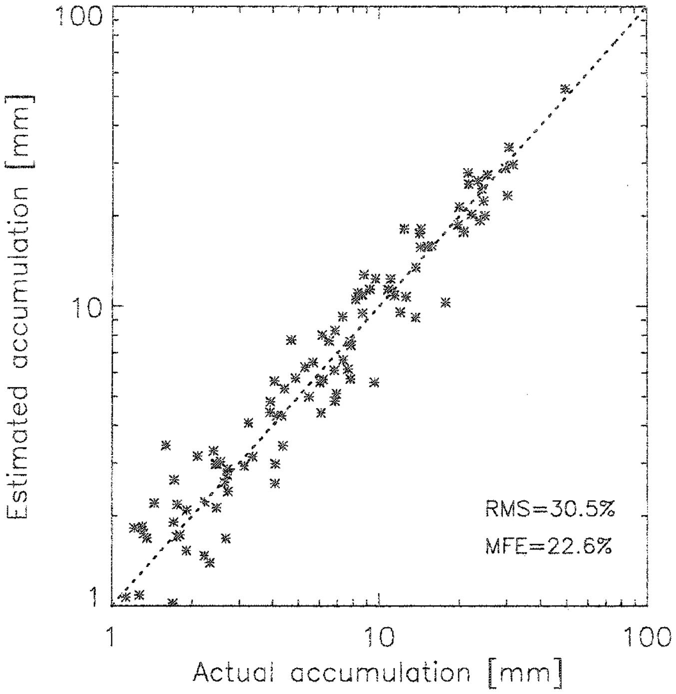

Fig. 3-9: Accumulations from single best Z-R relationship, C. Rica OSP.

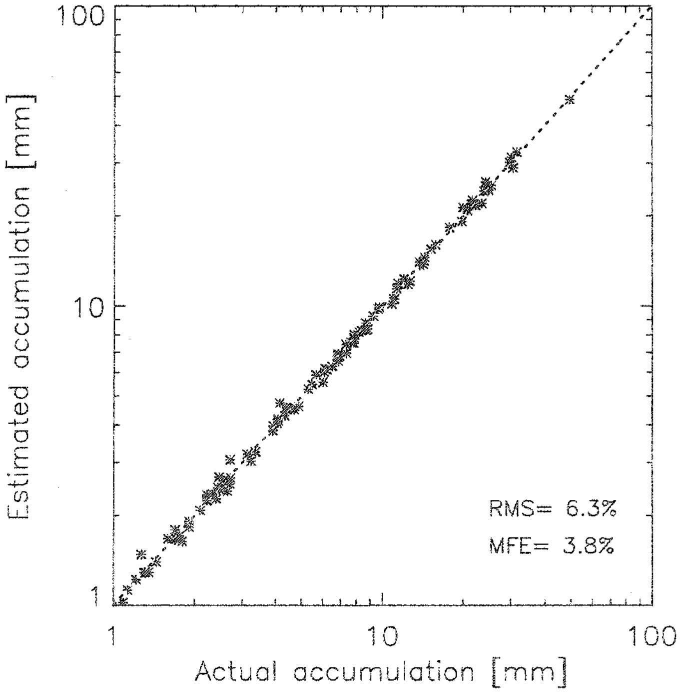

Fig. 3-10: Accumulations from daily-fitted Z-R relationships, C. Rica OSP.

3.8 Attenuation-estimated accumulations

Rain attenuation can be approximated by a moment of the DSD which is closer to rainfall rate than reflectivity. This means that the exponent of the diameter in the integral expression for K (around[*] 4.5) is nearer to the exponent of the diameter found in the expression for R (close to 3.67) than that found in the expression for Z (very close to 6.0).

Therefore, rainfall accumulations computed from attenuation-estimated rain rates are more precise than those from reflectivity-estimated rain rates. This fact is illustrated in Fig. 3-11 and Fig. 3-12, which display errors about 50% smaller than Fig. 3-7 and Fig. 3-9 respectively.

Surprisingly, these accumulations are not as good as those obtained from daily-fitted $Z-R$ relationships (Fig. 3-8 and Fig. 3-10). However, if the plots are constructed using accumulations from daily-fitted $K-R$ relationships as shown in Fig. 3-13 and Fig. 3-14, the errors decrease drastically. The attenuation method gives about half the errors of the reflectivity method.

Temperature affects the attenuation cross-section of raindrops at the X-band frequencies, particularly for bigger drops ($D > 2mm$). As can be seen in Fig. 2-5, a noticeable bulge-like feature develops for higher temperatures in the relationship between attenuation cross-section and particle diameter. Therefore, a power-law relationship between K and R is less appropriate and the variability of the drop size distribution more important. This causes the mean errors in our daily accumulations to increase with increasing temperature.

If the temperature profile is known, a correcting scheme can be implemented, but in the present work, we shall restrict ourselves to presenting the temperature-introduced errors in Fig. 3-15 and Fig. 3-16. Although the errors in K-estimated R increase with temperature they are still smaller than estimations from a single $Z-R$ relationship.

As discussed in Section 2.5, since attenuation is an integrated quantity we should not expect to be able to measure it with the same resolution as reflectivity. Therefore, the method proposed in Section 2.6 tries to estimate tuned $Z-R$ relationships for localized periods of time (or regions in space) by means of measuring the mean $Z-K$ relationship for each period (or region). In the next two sections we analyze the results and performance of this procedure.

---

[*] As explained in Section 2.1.3 the attenuation cross-sections cannot be very precisely approximated to a power-law of the diameters, however, from Fig. 2-1 it can be said that for the X-band, K is roughly proportional to the 4.5th moment of the DSD at T =10°C.

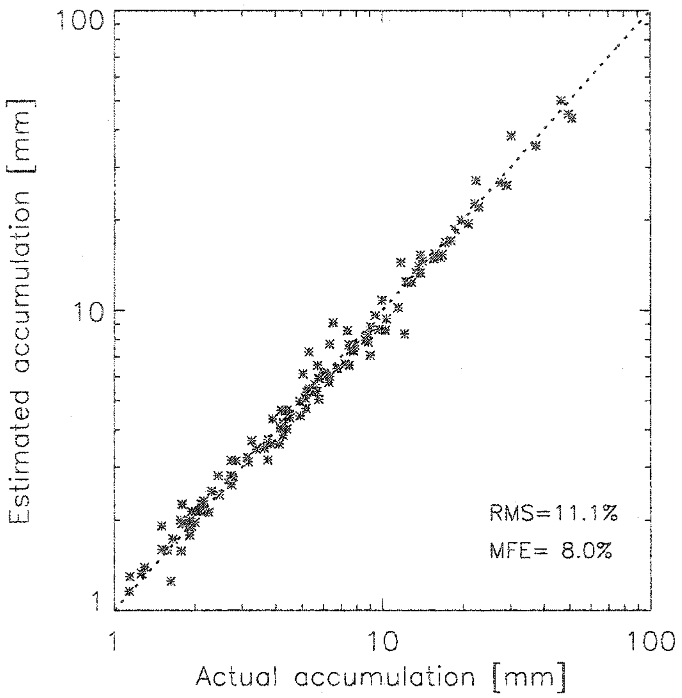

Fig. 3-11: Accumulations from fixed K-R relationship, McGill POSS.

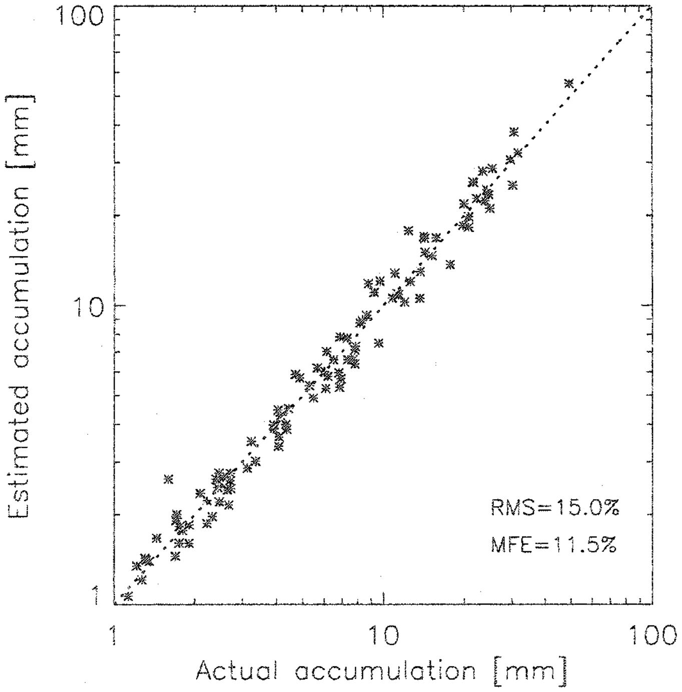

Fig. 3-12: Accumulations from fixed K-R relationship, C. Rica OSP.

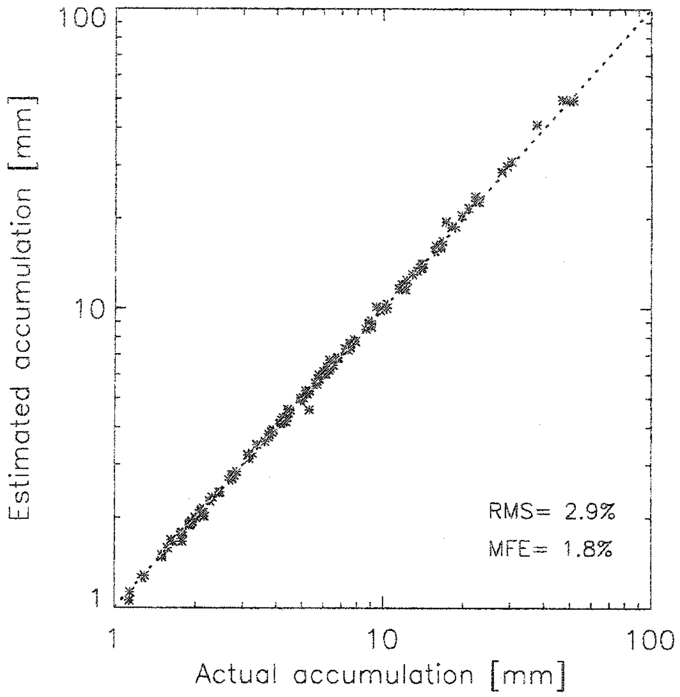

Fig. 3-13: Accumulations from daily-fitted K-R relationships, McGill POSS, 1994-2001.

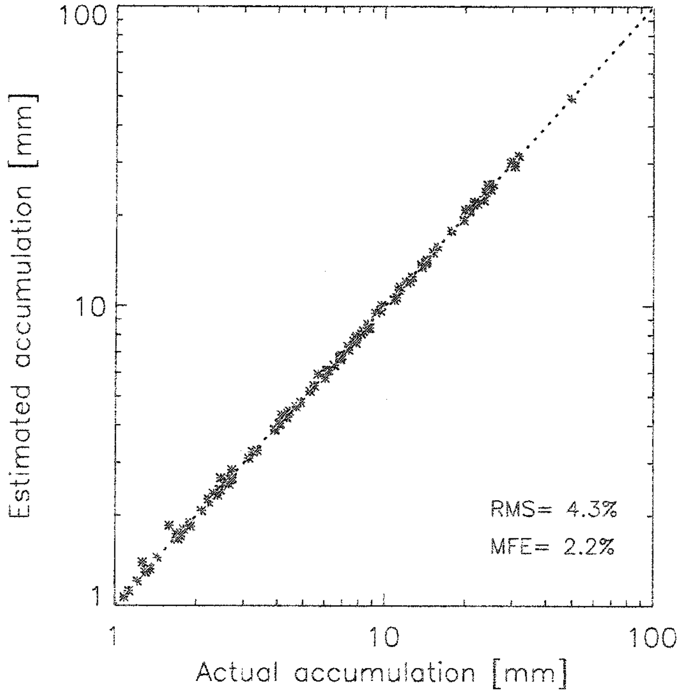

Fig. 3-14: Accumulations from daily-fitted K-R relationships, C. Rica OSP, 2000-2002.

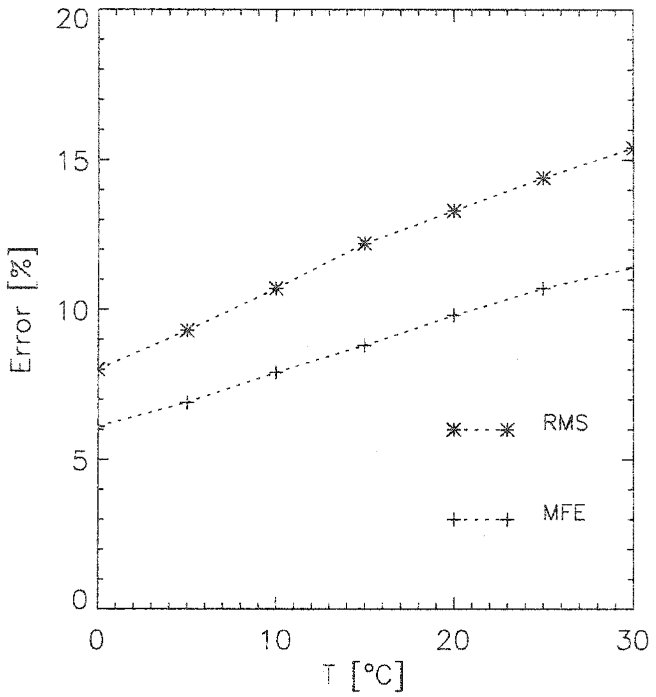

Fig. 3-15: Temperature dependence of errors from fixed K-R relationships, McGill POSS.

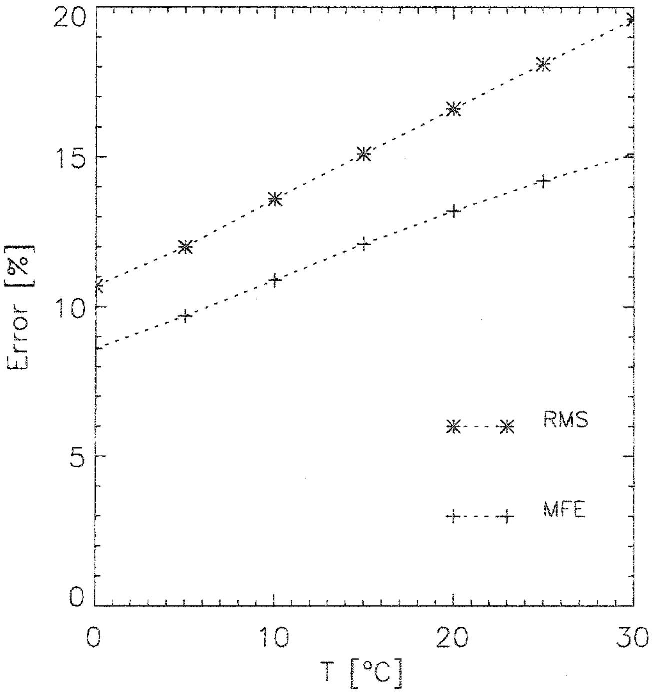

Fig. 3-16: Temperature dependence of errors from fixed K-R relationships, C. Rica OSP.

3.9 Algorithm results

The procedure described in Section 2.6 was applied to the McGill and Costa Rica disdrometer data series. The obtained results are plotted in Fig. 3-17 and Fig. 3-18. Estimated accumulations are plotted against actual accumulation measured by disdrometer, each point representing the total rainfall accumulation for a particular day.

The algorithm consists in finding best-fit $Z-K$ power-law relationships for reduced intervals of time (24 hours in this case) and then determining locally-tuned $Z-R$ relationships through a fixed $K-R$ relation. Therefore, a different $Z-R$ relationship was used in calculating the rain rate from reflectivity for each point in the plots. It is expected that the $Z-R$ relationships obtained in this way would produce better estimates of the rainfall rate.

Errors in the accumulations found from applying tuned relationships to reflectivity are indeed smaller than if a fixed relationship is used. Not surprisingly the magnitude of the error estimators closely resembles those obtained from directly computing R from K.

In the construction of both plots, the $K-R$ relationships from Fig. 3-3 and Fig. 3-4 were employed. However, the results obtained with relationships from the literature, after removing any introduced bias, are comparable to those of Fig. 3-17 and Fig. 3-18. An example is shown in Fig. 3-19 and Fig. 3-20, where the relationship $K = 0.021R^{1.16}$ from Atlas and Ulbrich (1974) was employed.

Table 3-3 and Table 3-4 summarize the results obtained by estimating daily accumulation using a variety of methods. Some important points to notice are:

- Rain rates estimated directly from the X-band specific attenuation factor (K) are about 50% more precise (in terms of daily rainfall accumulation) than those estimated from radar reflectivity.
- The use of daily-fitted relationships dramatically reduces the errors in the estimation of rain rate both from reflectivity and from specific attenuation.
- The use of daily-fitted $Z-R$ relationships produces errors that are even smaller than those from single (climatological) $K-R$ relationships.
- By daily tuning the $Z-R$ relationship from measured $Z-K$ relationships and a climatological $K-R$ relationship, errors are brought back to the same magnitude as if estimated directly from attenuation. That is, we get around a 50% improvement in accuracy.

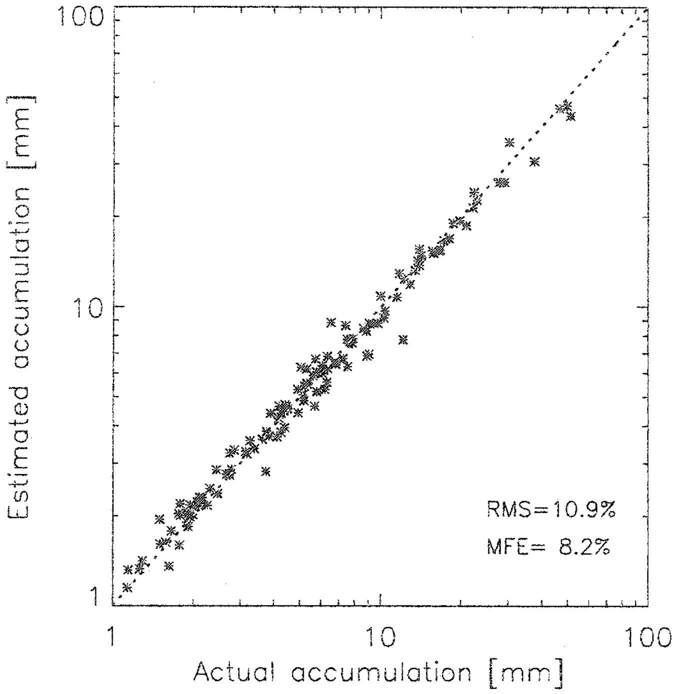

Fig. 3-17: Accumulation from daily-tuned Z-R relationships, McGill POSS.

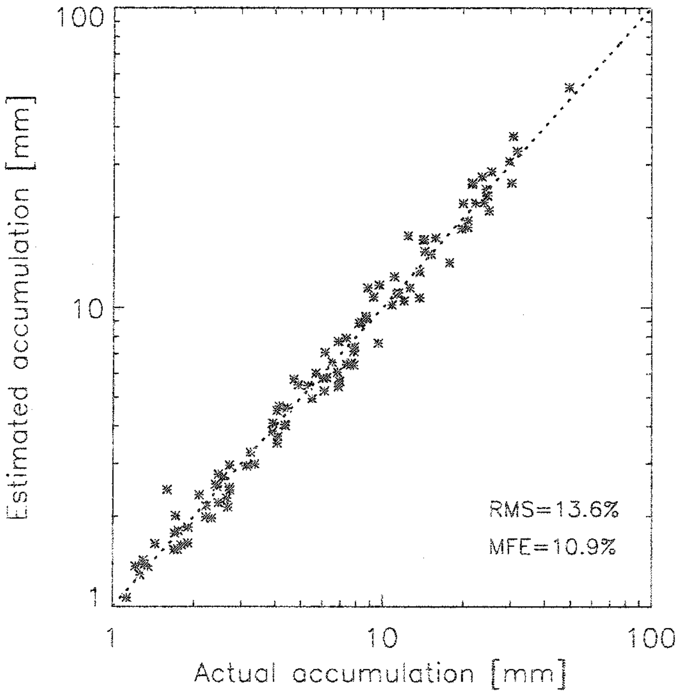

Fig. 3-18: Accumulation from daily-tuned Z-R relationships, C. Rica OSP.

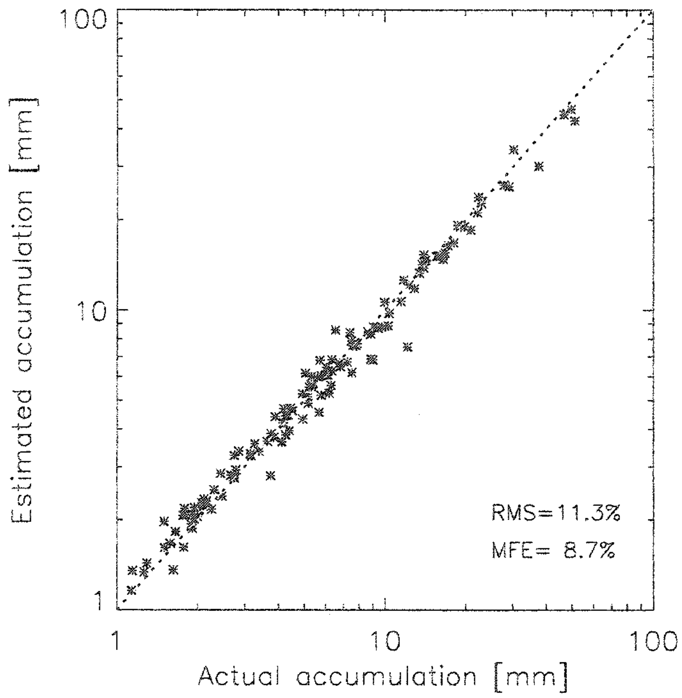

Fig. 3-19: Same as Fig. 3-17, but using K-R relationship from Atlas and Ulbrich (1974).

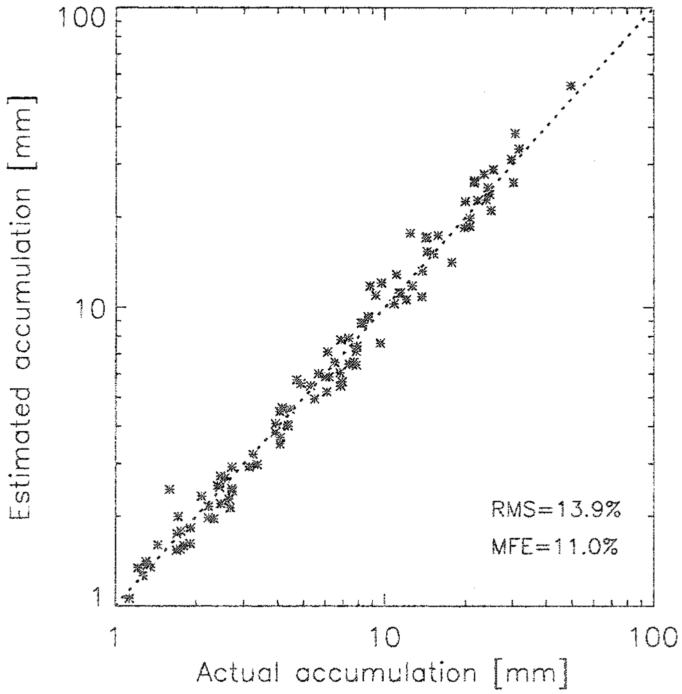

Fig. 3-20: Same as Fig. 3-18, but using K-R relationship from Atlas and Ulbrich (1974).

Method	***RMS Error [%]***	***Mean Fract. Error [%]***
Fixed Z-R relation	*28.4*	*21.7*
Fixed K-R relation	*11.1*	*8.0*
Daily Z-R relation	*5.1*	*3.6*
Daily K-R relation	*2.9*	*1.8*
Tuned Z-R relation	*10.9*	*8.2*

Table 3-3 Summary of precipitation-estimation methods for McGill POSS.

Method	***RMS Error [%]***	***Mean Fract. Error [%]***
Fixed Z-R relation	*30.5*	*22.6*
Fixed K-R relation	*15.0*	*11.5*
Daily Z-R relation	*6.3*	*3.8*
Daily K-R relation	*4.3*	*2.2*
Tuned Z-R relation	*13.6*	*10.9*

Table 3-4 Summary of precipitation-estimation methods for C. Rica OSP.

3.10 Performance of the tuning algorithm

Fig. 3-21 through Fig. 3-24 compare the best-fitted and algorithm-retrieved parameters of daily $Z-R$ relationships for both datasets. In these figures the values of the daily best-fit parameters are plotted against the same parameters as retrieved by the tuning algorithm. A perfect retrieval would be indicated by all the points lying in the 45 degree line (dotted line).

In general the tuning algorithm performs reasonably well for the retrieval of both the coefficient a and the exponent b of the $Z-R$ relationship ($Z=aR^b$). The major differences occur for the higher values of the coefficient (a > 400). An obvious deviation toward lower values of a is observed in Fig. 3-21 and Fig. 3-23. This indicates that the algorithm fails to recover high values of the coefficient. Apparently, the maximum value of a that the algorithm can recover is around 400. It is also apparent that the scatter between the best-fit parameters and the parameters retrieved by the algorithm is smaller for the coefficient than for the exponent.

The accumulations obtained from daily-tuned $Z-R$ relationships are slightly better than direct accumulations from a single $K-R$ relationship (see Table 3-3 and Table 3-4). No clear explanation exists for this unexpected gain. However, the improvement is small enough to be considered within the errors of the algorithm.

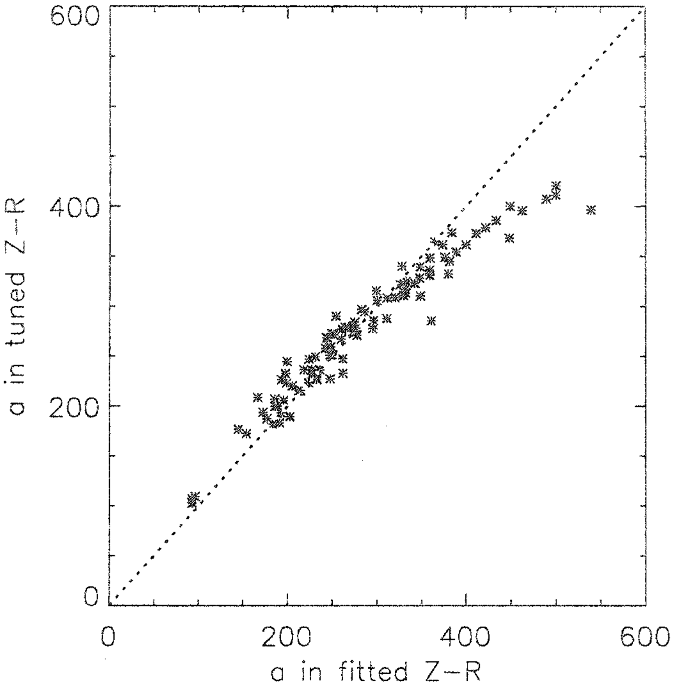

Fig. 3-21: Retrieval of the coefficient a of daily Z-R relationships, McGill POSS.

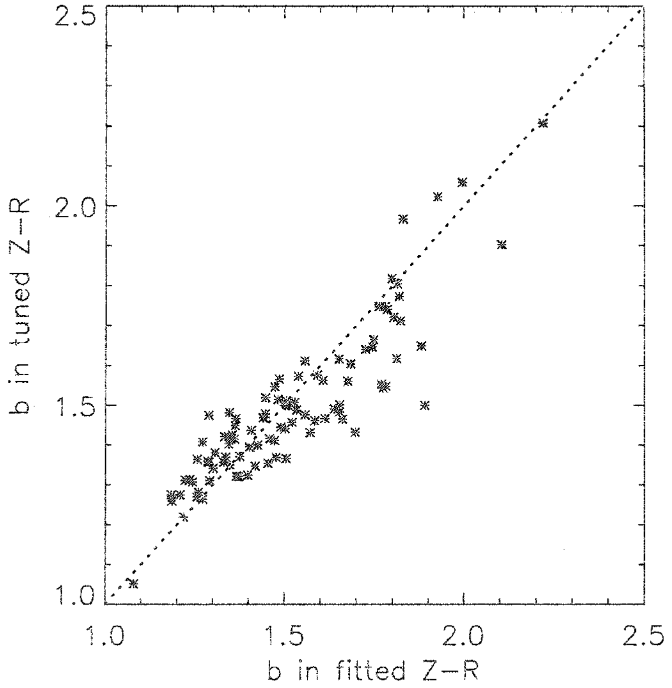

Fig. 3-22: Retrieval of the exponent b of daily Z-R relationships, McGill POSS.

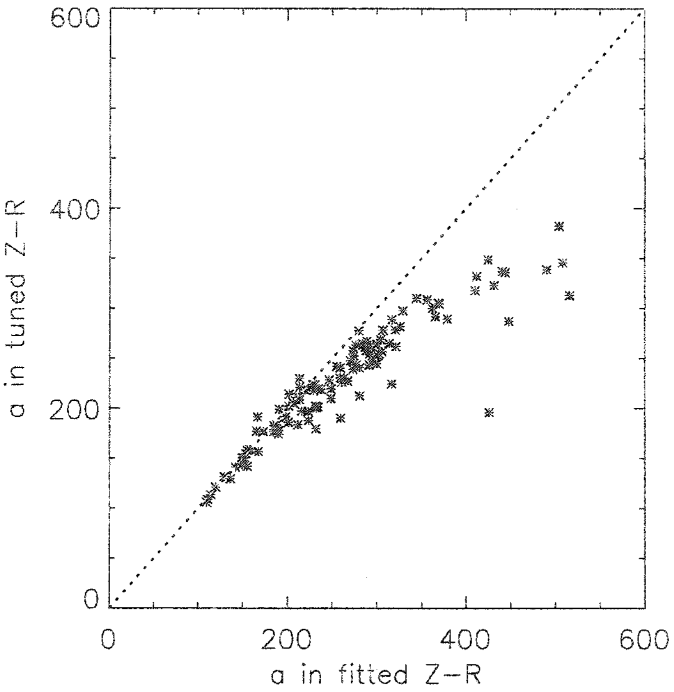

Fig. 3-23: Retrieval of the coefficient a of daily Z-R relationships, C. Rica OSP.

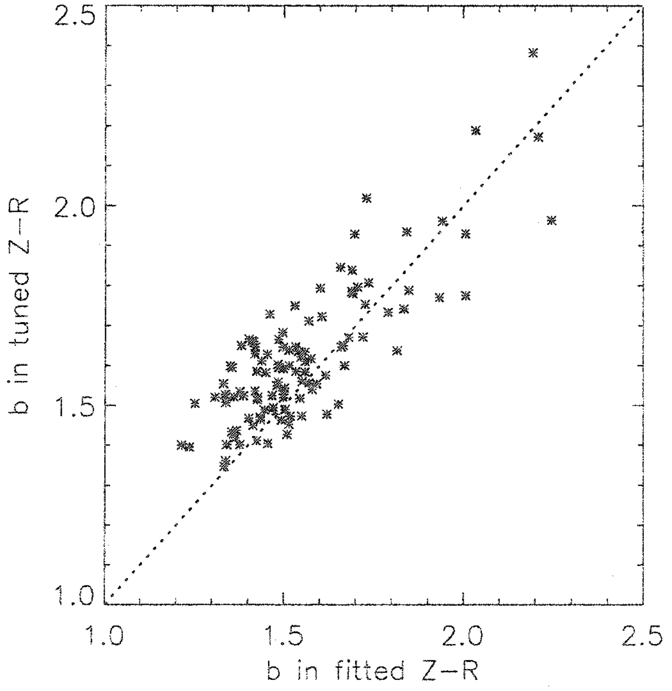

Fig. 3-24: Retrieval of the exponent b of daily Z-R relationships, C. Rica OSP.

3.11 Calibration errors

Any systematic error introduced by the radar in the measurement of reflectivity would be reflected as an error in rainfall accumulations when rain rates are calculated directly from Z. However, the $Z-R$ relationships provided by the tuning algorithm are estimated from measured $Z-K$ relationships and since attenuation is not affected by calibration errors the resulting $Z-R$ relationships are automatically corrected for calibration errors in reflectivity. Consequently, the tuning algorithm has the property of being largely insensitive to radar calibration errors.

In order to illustrate this particularity of the tuning algorithm, another simulation was done using the POSS and OSP datasets described in Section 3.3. This time a random calibration error was introduced for each individual day in the data series. The calibration error was kept constant within each particular day, but was made to vary randomly from day to day.

Table 3-5 and Table 3-6 show the results of the simulation. The displayed numbers are the root mean square error as well as the mean fractional error for various magnitudes of the calibration error. In the simulations, the calibration error was selected randomly but bounded within $\pm 1\,dB$, $\pm 2\,dB$ and $\pm 3\,dB$ respectively. The first row in both tables is identical to the results obtained in Fig. 3-7, Fig. 3-17 for POSS and Fig. 3-9, Fig. 3-18 for OSP.

The resistance of the tuning algorithm to calibration errors is demonstrated by the fact that although the errors incurred by the use of a single $Z-R$ systematically increase with increasing calibration errors, the errors produced by the tuning algorithm remain remarkably stable.

Method	***Fixed Z-R relation [%]***	***Tuned Z-R relation [%]***
No calibration error	*28.4 (21.7)*	*10.9 (8.2)*
±1dB calibration error	*29.7 (22.6)*	*11.1 (8.3)*
±2dB calibration error	*33.6 (25.1)*	*10.8 (8.1)*
±3dB calibration error	*49.5 (36.2)*	*10.8 (8.1)*

Table 3-5 Performance of tuning algorithm with calibration errors for McGill POSS.

Method	***Fixed Z-R relation [%]***	***Tuned Z-R relation [%]***
No calibration error	*30.5 (22.6)*	*13.6 (10.9)*
±1dB calibration error	*31.1 (23.6)*	*13.7 (10.9)*
±2dB calibration error	*35.1 (25.3)*	*13.6 (10.8)*
±3dB calibration error	*50.7 (34.8)*	*13.9 (11.0)*

Table 3-6 Performance of tuning algorithm with calibration errors for C. Rica OSP.

4 Radar measurements

4.1 Measuring attenuation with dual-wavelength radars

Dual-wavelength radars can be used to measure the differential attenuation between their two frequencies. Usually one of their frequencies can be regarded as non-attenuating. Then the differential attenuation is equal to the attenuation experienced by the attenuating wavelength.

If we assume Rayleigh scattering at both frequencies, which is usually a good approximation for wavelengths larger than $3cm$ [Atlas and Ulbrich, 1974], the back-scattering cross-section of a raindrop of diameter D is:

$$\sigma_b \cong \frac{\pi^5 |K|^2}{\lambda^4} D^6 \tag{4-1}$$

Then the effective reflectivity of a target:

$$Z_e = \frac{1}{V} \frac{\lambda^4}{\pi^5 |K|^2} \sum_{i=1}^{N} \sigma_{bi} \tag{4-2}$$

is independent of the illuminating wavelength and very close to the meteorologically defined reflectivity value:

$$Z = \frac{1}{V} \sum_{i=1}^{N} D_i^{\,6} \tag{4-3}$$

This reflectivity definition is independent of the radar wavelength. Therefore, the total path attenuation from the radar to a particular point can be obtained by subtracting the reflectivity measured by the attenuated wavelength from that of the non-attenuating channel. The mean specific attenuation factor is simply the path attenuation divided by the path length.

4.2 Errors involved

In the simulations of the previous chapter it was assumed that the attenuation factor could be measure with no error. This is not true since there are many factors that complicate the retrieval of attenuation.

First of all, there is an inherent error in the estimation of reflectivity from the fluctuating power returned to the radar. This error arises from the fact that meteorological targets are composed of randomly distributed particles which act as random-phase scatterers. Therefore, a particular echo returned to the radar is random in nature and carries little information. The averaging of many individual samples is required to estimate the mean intensity of a meteorological target. However, scanning radars are constrained by their pulse repetition frequency, antenna motion and other factors that limit this average to a relatively small number of independent samples.

A second factor is that with increasing rain intensity a greater concentration of bigger drops would be present in precipitation. Although these drops are always Rayleigh scatterers at the S-band, the approximation is not as good for shorter wavelengths such as the X-band. The inaccuracy of the Rayleigh approximation causes the reflectivity measured with the two wavelengths to be different. This is called Mie-effect, for the full Mie equations are required to correctly evaluate the scattering cross-section of bigger drops at the short wavelength.

The polarization employed in each channel of a dual-wavelength radar is another factor to be considered. For example, the MRL-5 radar (see Appendix D) has two different polarizations: horizontal for the S-band and vertical for the X-band. As a result, since raindrops flatten while falling through the atmosphere, a difference in reflectivity exists between these two polarizations.

Furthermore, the antenna or antennas used for each wavelength might not illuminate exactly the same volume of space. This can be due to misaligned antennas, unmatched pulse length, differences in beam-width and shape, or even dissimilarity in antenna side-lobes. If this is the case, the two wavelengths would return information from two different regions in space. This error can nevertheless be reduced by spatial integration in the post-processing stage.

4.2.1 Finite number of independent samples

The problem of calculating the error incurred in estimating reflectivity with a weather radar has been extensively studied [Marshall and Hitschfeld, 1953; Smith, 1964; Sirmans and Doviak, 1973]. The echo from meteorological targets varies randomly due to the random reshuffling of the collection of scatterers. Therefore, multiple independent samples are needed in order to properly estimate the mean value of echo intensity, i.e. the reflectivity.

Marshall and Hitschfeld (1953) give simple formulas for the probability function, most probable value, mean value, and standard deviation for the most commonly employed radar receivers. These equations are summarized in Table 4-1. Smith (1964) presents a thorough discussion on the topic with more reasonable assumptions regarding the probability distribution of the intensity of actual atmospheric targets. Rodriguez (1998) analyzes the subject in the context of MRL-5 radars.

In general, the error in the estimation of reflectivity is proportional to the inverse of the square root of the number of independent samples, e.g. for a logarithmic receiver, the error in the estimation of Z is:

$$e_Z^{Log}(k) \cong 10 \times \frac{\pi \log e}{\sqrt{6}} \frac{1}{\sqrt{k}} \qquad [dB] \qquad (4\text{-}4)$$

where k is the number of independent samples, and the value $\frac{\pi \log e}{\sqrt{6}}$ is the error in estimating the mean value of Z from a single independent sample with a logarithmic receiver (Table 4-1). Fig. 4-1 shows a plot of $e_Z^{Log}(k)$.

Weather radars usually are capable of measuring reflectivity with an error (e_Z^{Log}) in the order of $1\,dB$. Consequently, the minimum measurable two-way attenuation along a radial path would be $1\,dB$ divided by the path length, e.g. for an $8\,km$ path, the minimum measurable two-way attenuation factor is $0.125\,dBkm^{-1}$.

	Linear receiver	***Quadratic receiver***	***Log. Receiver***
Probability distribution	$\frac{2A}{\overline{A^2}} e^{-A^2/\overline{A^2}}$	$\frac{1}{\overline{I}} e^{-I/\overline{I}}$	$m e^{\left(m(L-L_0)-e^{m(L-L_0)}\right)}$ $m = \ln 10$
Most probable value	$\sqrt{\frac{\overline{A^2}}{2}}$	0	$L_0 = \log \overline{I}$
Mean value	$\frac{\sqrt{\pi \overline{A^2}}}{2}$	$\overline{I}$	$L_0 - 0.251$
Standard deviation	$\frac{\sqrt{(4-\pi)\overline{A^2}}}{2}$	$\overline{I}$	$\frac{\pi \log e}{\sqrt{6}}$

Table 4-1 Properties of the probability distributions of individual echoes.

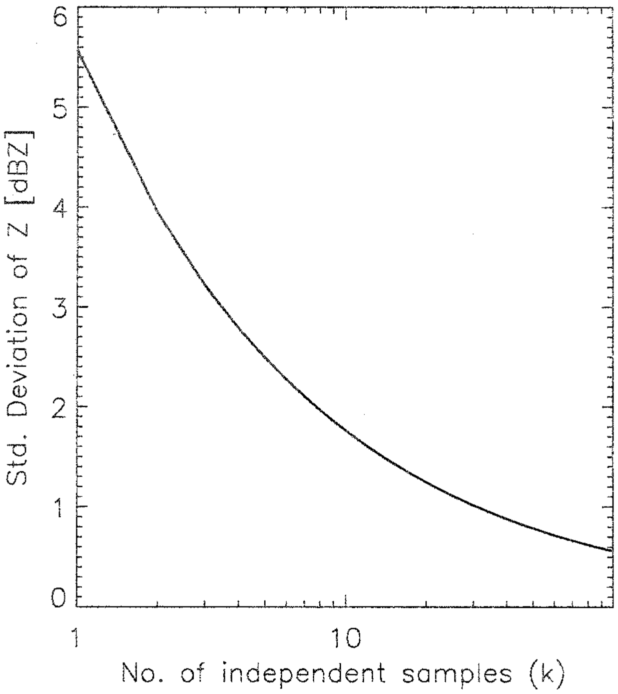

Fig. 4-1: Error in the estimation of reflectivity for a logarithmic receiver.

4.2.2 Mie-effects, polarization and differential reflectivity

Large raindrops behave as non-Rayleigh scatterers at the shorter wavelength of dual-wavelength radars. Therefore, for higher precipitation rates we should expect a difference between our two measured reflectivities. In order to evaluate these errors, as well as those produced by having distinct polarizations for the two wavelengths, we can calculate the difference in radar-measured reflectivity using a disdrometer dataset (the POSS data series described in Section 3.3) and a scattering model (see Section 3.4).

Fig. 4-2 shows the difference in reflectivity caused by Mie scattering in the X-band when compared to measured S-band reflectivity. The plot was constructed for horizontal polarization. However, it is very similar for vertical polarization. The thick solid line in the plot illustrates the difference in reflectivity that would be produced by Marshall-Palmer drop size distributions.

Fig. 4-3 shows the differential reflectivity measured between horizontal and vertical polarizations caused by the deformation of falling raindrops, usually denoted as Z_{DR}. The data for Fig. 4-3 come from the S-band. The picture for the X-band is similar. The solid line is again the differential reflectivity that would be produced by Marshall-Palmer drop size distributions.

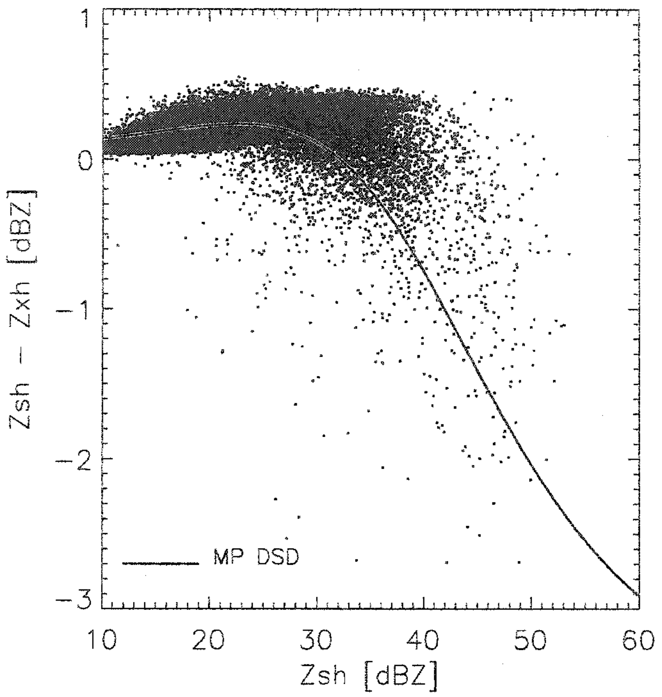

Fig. 4-2: Difference in reflectivity between S- and X-band due to Mie-effects.

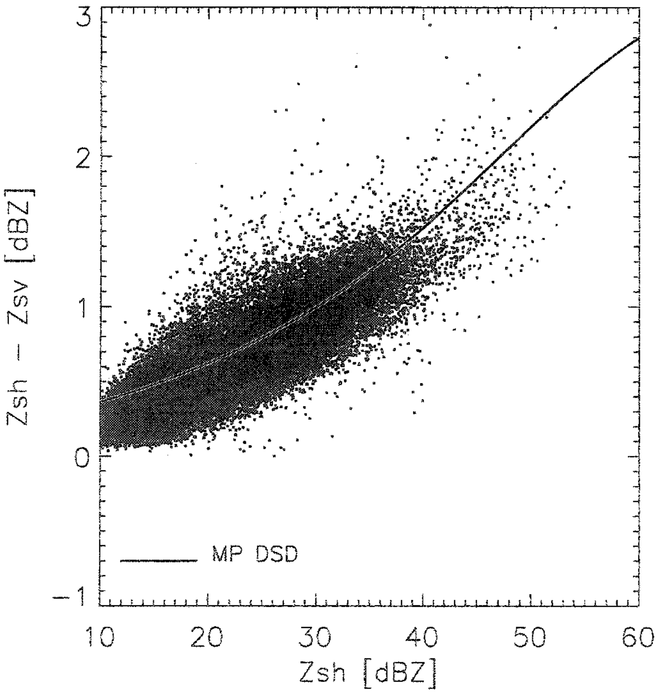

Fig. 4-3: Differential reflectivity for the S-band.

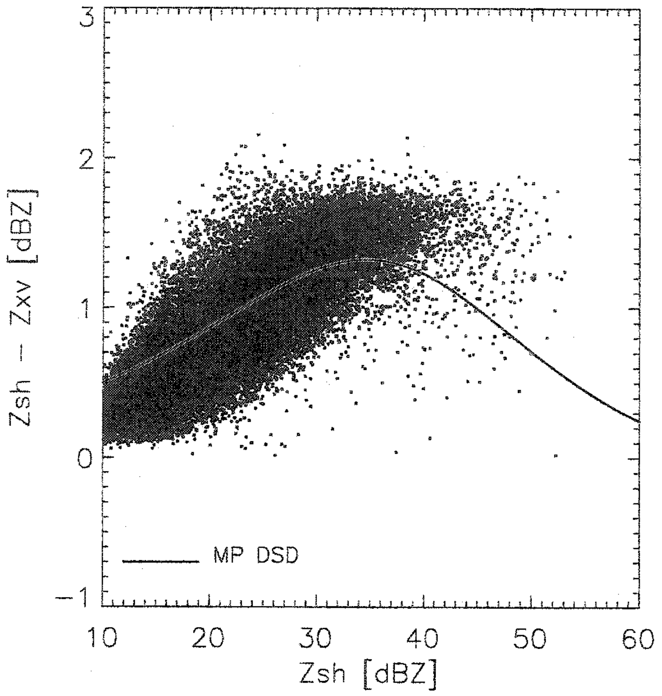

Fig. 4-4: Difference in reflectivity due to Z_{DR} and Mie-effects: Canceling configuration.

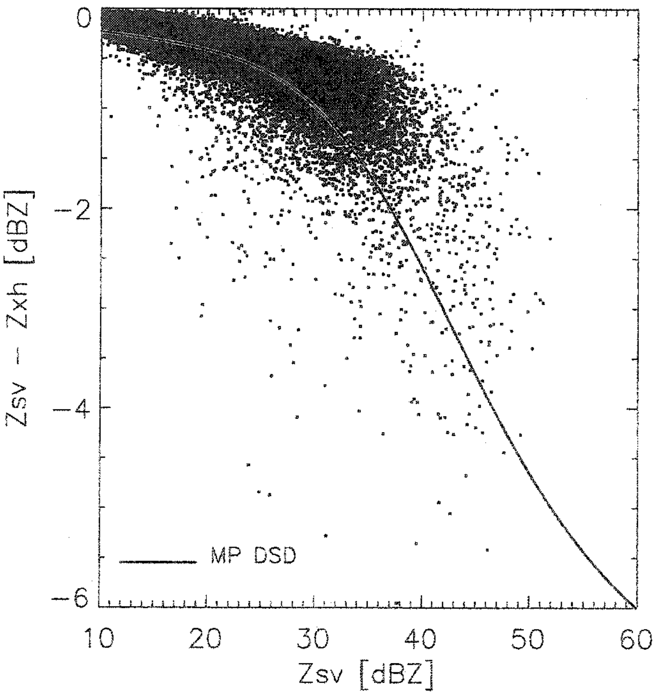

Fig. 4-5: Difference in reflectivity due to Z_{DR} and Mie-effects: Additive configuration.

If both wavelengths have the same polarization only Fig. 4-2 applies. However, the solution to placing two wavelengths co-linearly in the same antenna with similar beam patterns often requires them having different polarizations. Two possible configurations exist in this case. In one of them Mie-effects and Z_{DR}-effects tend to partially cancel each other as in Fig. 4-4, while in the other configuration these effects add up as shown in Fig. 4-5.

4.2.3 Beam-matching and co-linearity

If the two wavelengths of a dual-wavelength radar do not have the same antenna beam-width, they will be measuring the reflectivity of different volumes of space at any given time. The same is also true if the two beams do not point in exactly the same direction. In this section we evaluate the severity of errors introduced in these two cases.

For this goal we used the high-resolution reflectivity field represented in Fig. 4-6. This reflectivity field was acquired with a vertically-pointing radar operated in the Marshall Radar Observatory of McGill University. The measured time-series of the vertical profile of reflectivity were considered as frozen in time and corresponding to a spatial-cut across a precipitation field. The conversion from time- to space-series was made usign a wind of $16\,ms^{-1}$ measured with a wind profiler.

A post-detection integration cell of $1\,km \times 1°$ was assumed in the radar. Only the data within the dotted boundary in Fig. 4-6 were used in order to prevent bright-band contamination and boundary effects. The resolution is $37.5\,m$ in the vertical axis and around $40\,m$ in the horizontal.

In the simulation, a dual-wavelength radar is placed in front of the reflectivity field (looking from outside the page). For each beam-width an equivalent Gaussian weighting function is convoluted with the field and the reflectivities obtained in this way are compared.

Fig. 4-7 shows the errors caused by beam-misalignment for four different beam-widths. dA is the angular difference between the two pencils of radiation. The error is measured as the standard deviation of the absolute difference between the Gaussian mean of the two pencils.

The error is found to be more important for small beam-widths. But even for intermediate beam-widths as in the MRL-5 (1.5°) a half beam-width misalignment would introduce an average $1.5\,dB$ error. These alignment errors are difficult to spot in the post-processed field due to angular averaging, but are easy to correct (by adjusting the misaligned antennas) if careful measurements are taken of ground echoes that are sharp in azimuth (e.g. a tall distant chimney).

Fig. 4-8 and Fig. 4-9 display the mean bias and standard deviation between two different antenna beams measuring reflectivities simulated from the reflectivity field in Fig. 4-6. An integration of reflectivity in cells of $1\,km \times 1°$ was done prior to the comparison.

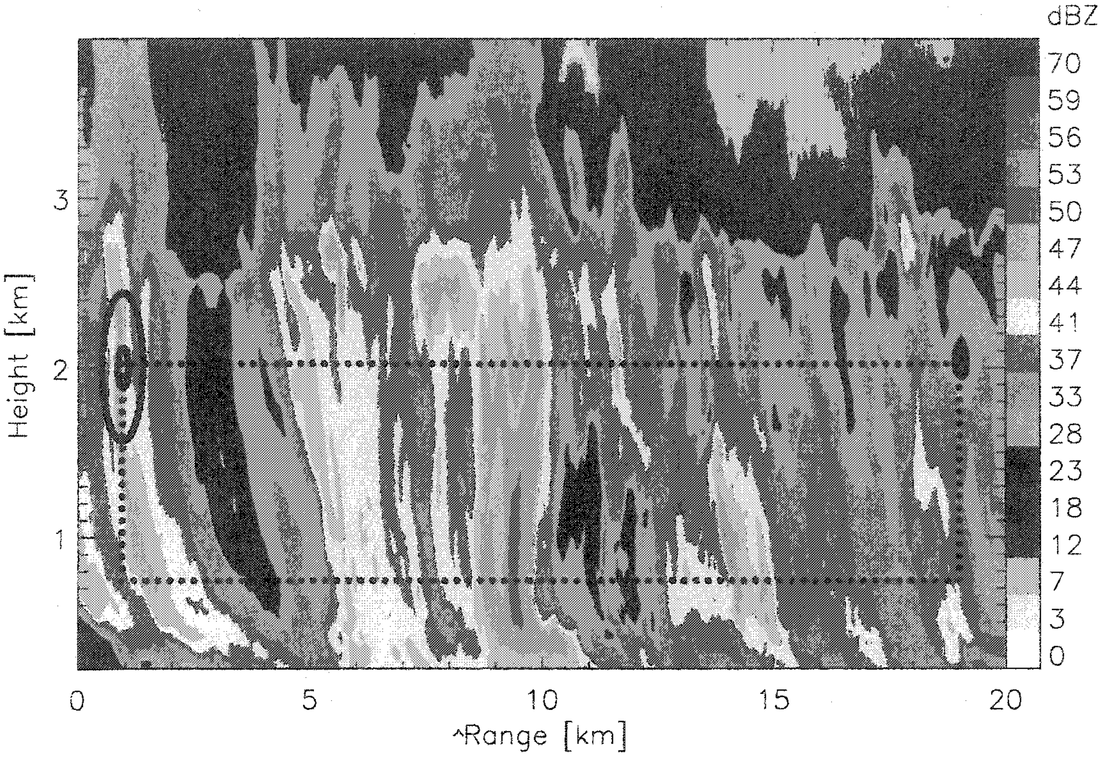

Fig. 4-6: VPR data. The ellipses represent the footprint of 0.86° and 0.26° beams at 60km

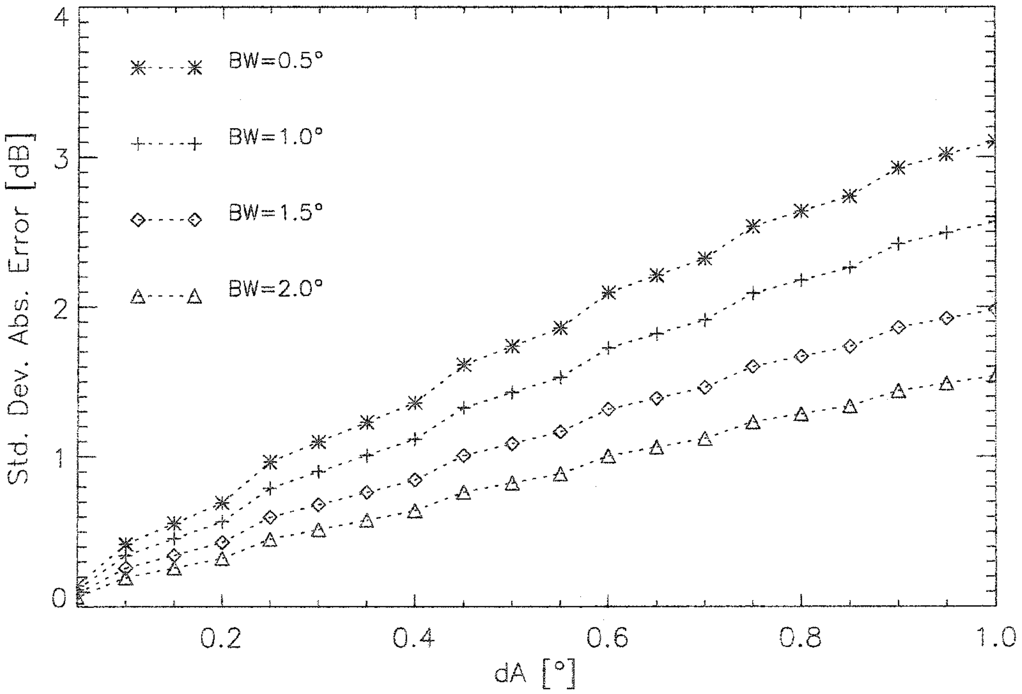

Fig. 4-7: Errors due to beam-misalignment at a range of 60km.

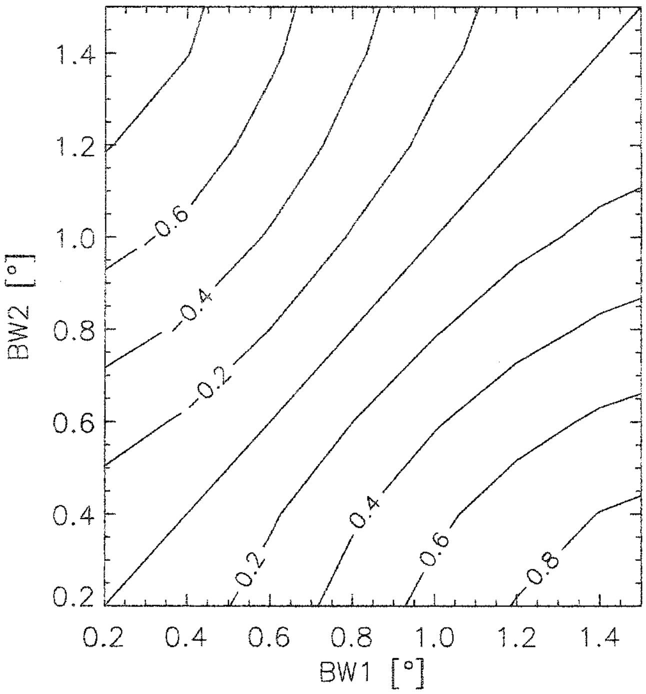

Fig. 4-8: Mean bias [dBZ] due to a difference in beam-widths at a range of 60km.

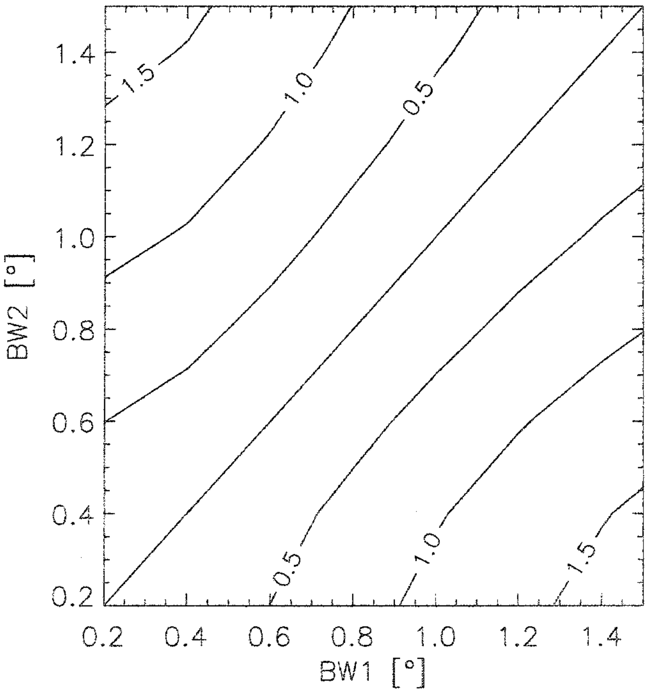

Fig. 4-9: Same as Fig. 4-8 but standard deviation [dBZ] of absolute error.

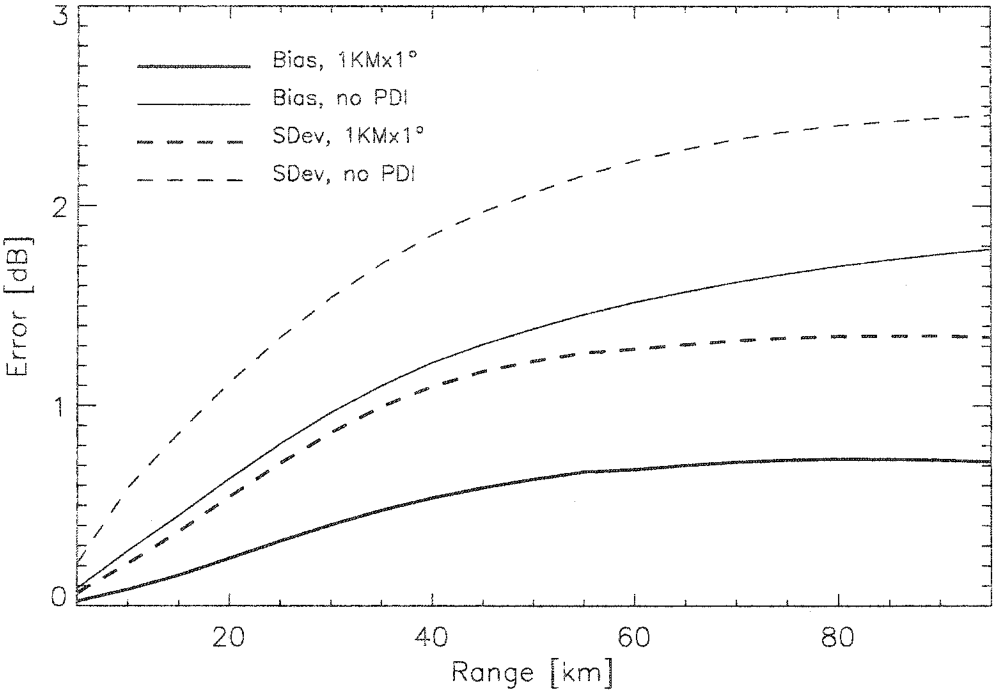

Fig. 4-10: Influence of post-detection integration on beam-matching errors.

The magnitude of the bias and the standard deviation are greatly reduced by this post-detection spatial integration (azimuth and range). An example is presented in Fig. 4-10, which shows the errors incurred in using beam-widths that follow the pattern of the MRO radar. The large beam is 0.86° while the small one is 0.26°. The actual integration cell size of the MRO radar ($1\,km \times 1°$) was used. In the plot, the thick lines represent the post-detection integrated signal while the thin lines represent the signal without integration. In each case the solid lines indicate the mean bias and the dashed lines show the standard deviation of the mean absolute error.

The mean bias is a systematic error that needs to be corrected. This is done by matching the two reflectivities of the dual-wavelength radar at the beginning of the each path segment. Since segments are always short in length, the change of the mean bias with range is considered insignificant. Random errors can only be corrected by averaging. For the case of the MRO radar, the beam-width disparity produces a $0.5\,dB$ to $1.5\,dB$ average random error in the distance range from $20\,km$ to $80\,km$. This is the distance range where we compute attenuation.

The error values presented in this section depend on the structure of precipitation and should only be used as an indication of how important beam-matching and beam co-linearity are. Other sources of error such as unmatched pulse width and antenna side-lobes were not explored here, but they can only make the situation worse.

4.3 Dataset

At the beginning of this work, we expected data from the dual-wavelength MRL-5 radar in Camagüey, Cuba to be available. Data from MRL-5 radars is appealing because of their matched, co-lineal beams and the particular polarization of their two frequencies. However, a number of problems have plagued the Camagüey radar's newly digitized X-band channel during the spring and summer of 2002, preventing it from operating. Further repairs were postponed until after the current hurricane season.

Nevertheless, a limited dataset acquired at the J. S. Marshall Radar Observatory (MRO) of McGill University can be used to illustrate some aspects of the theory presented in this thesis. This dataset consists of dual-wavelength reflectivity measurements with the MRO main scanning radar (see Appendix C) and drop size distributions measured with a POSS sensor situated thirty kilometers away from the radar on the roof of a downtown Montreal building. A total of ten days of precipitation were analyzed, but only in two of them was the precipitation strong enough to produce significant attenuation and the precipitation passed over the POSS disdrometer.

The work with actual radar data permitted the development and testing of an algorithm for the extraction of mean reflectivity and attenuation pairs. These data pairs are then used to calculate the mean $Z-K$ relationship required by the tuning or calibration algorithms (see Section 4.6).

4.4 Characteristics of the MRO dataset

In the dual-wavelength MRO radar both wavelengths share the same parabolic antenna[*]. A major problem with this approach is that the antenna produces very different beam-widths for the two frequencies. The half-power ($-3\,dB$) beam-width for the S-band is 0.86° while it is only 0.26° for the X-band. Consequently, in each pulse the illuminated volume is bigger for the S-band than for the X-band. This error is somewhat reduced by the fact that data is averaged in cells of $1\,km \times 1°$.

At the time of the measurements the effective pulse repetition frequency of the S-band for reflectivity was particularly low, at only $36\,Hz$. Even if every sample is considered to be independent, it produces a total of only eight independent samples for each resolution volume of $1\,km \times 1°$. From Fig. 4-1 the error in the estimation of reflectivity was around $2\,dB$. This imposes

---

[*] An X-band channel was temporarily added to the S-band dish.

a lower limit to the attenuation that can be measured. For an $8\,km$ path length it would be $0.25\,dBkm^{-1}$, a value that on average requires reflectivities higher than $37\,dBZ$.

The X-band unit had a much higher pulse repetition frequency (see Appendix C). This makes the estimation of reflectivity more accurate but introduces the problem of second-trip echoes. Second-trip echoes originate when reflections of a previous pulse arrive at the receiver at the same time as those from the current pulse. These previous-pulse echoes come from distant objects that are intense enough to produce a detectable signal. Second-trip echoes contaminate the reflectivity field and need to be eliminated before computing the attenuation.

Ground-clutter is another factor affecting dual-wavelength measurements of attenuation. We have chosen to exclude all clutter-contaminated regions from the analysis. This was done through a fixed ground-clutter mask measured as an average of many clear-day echoes with the S-band. The same mask is used for the X-band.

A minor problem with the MRO dataset is that the start of the S- and X-band fields is not synchronized. Apparently, the measurements did not start at exactly the same time for both channels. The most common situation is the start of the X-band field lagging behind the S-band. This situation is corrected by taking the cross-correlation between the two fields at different lags and correcting for the one that produces the best correlation.

4.5 Elevation angles

The MRO radar has a fixed scanning strategy with 24 elevation angles ranging from 0.5° to 34.4° distributed in two subsets of 12 angles (see Appendix C). A full volume scan takes five minutes to execute, but each subset is scanned every 2.5 minutes.

The lowest elevation angles are very contaminated with ground clutter while higher elevation angles normally hit the melting layer after only a short distance. Besides this, in the radar configuration at the time of the observations, the S-band data for the lowest elevation angles was suppressed up to a distance of about $30\,km$ from the radar to protect the radar receiver from very intense reflections from close objects.

A compromise had to be reached. During the two days of data collection the height of the bright band was always above $3.8\,km$. Therefore data from three elevations angles were use in this study: 1.4°, 1.8° and 2.2°. These antenna elevations allow for attenuation measurements up to a range of $80\,km$ without reaching the melting layer. A more careful choice of elevation angle and ranges can produce additional data points.

4.6 Extraction of Z and K pairs

To extract the mean reflectivity-attenuation relationship from dual-wavelength data we need Z and K pairs that we then use to fit a power-law relationship. These Z, K pairs should be the average value of a path as short as possible.

However, the minimum path length is limited by the minimum attenuation that must be measured in order to circumvent the numerous errors discussed in Sections 4.2 and 4.4.

A simple equation can be used to calculate the X-band attenuation factor up to range r:

$$K = \frac{1}{r}(Z_S - Z_X + C_Z) \qquad [dBkm^{-1}, Z \text{ in } dBZ] \quad (4\text{-}5)$$

C_Z is a factor that compensates the mean bias introduced by the Mie and differential reflectivity effects described in Section 4.2.2. C_Z depends on reflectivity as well as on the polarization of the two frequency channels of the radar.

There is a problem with this equation. The initial range r_0 cannot be zero because all radars are surrounded by a near-field (*Fresnel*) region in which the angular field distribution depends on the distance from the radar antenna. The boundary between this region and the far-field (*Fraunhofer*) region in which the angular field distribution is independent of the distance from the antenna is not clear. A value for the far-field range is given by Balanis (1997):

$$r_F = 2\frac{D^2}{\lambda} \quad (4\text{-}6)$$

D is the maximum dimension of the antenna, the diameter in the case of a parabolic dish.

Since this far-field range depends on wavelength, the S- and X-band reflectivities should not be expected to match below this distance. For the MRO radar $r_F \approx 2\,km$ for the S-band channel and $r_F \approx 6\,km$ for the X-band channel. As a consequence $r_0 \geq 10km$ was chosen.

To account for X-band attenuation prior to r_0 we need to match Z_X to Z_S at this point. As a consequence the X-band channel is not required to be well calibrated. Our equation after matching the reflectivities at the beginning of the path becomes:

$$K = \frac{1}{\Delta r}(\Delta Z_S - \Delta Z_X + C_Z) \quad (4\text{-}7)$$

The error incurred in estimating the S-band reflectivity in the MRO radar is about $2\,dBZ$ considering the independent samples alone. When additional error sources are included the error of $(\Delta Z_S - \Delta Z_X + C_Z)$ might well be above $4\,dBZ$. Consequently, we must use total attenuation values in excess of $4\,dB$.

An adequate balance of high total attenuation and short path lengths can only be obtained for a minimum value of reflectivity. In our case we choose $8\,km$ path length and a minimum reflectivity of $40\,dBZ$. These values produce at least $3.5\,dB$ of total attenuation on average.

4.7 Radar data

Due to the large number of error sources present in the MRO dataset and also because of the limited size of the dataset, no local tuning of $Z-R$ relationships was attempted. Instead our effort was restricted to use the extra information provided by attenuation as a ways of externally calibrating the radar station.

The next Chapter discusses the causes and implications of the puzzling pattern that appears in climatological relationships involving attenuation and that was presented in Section 3.5. Then, Chapter 6 presents the results of the calibration algorithm applied to the MRO dataset.

5 Data interpretation

5.1 Climatological relationships

Long-time series of disdrometer measurements coupled with a scattering model can be used to derive climatological relationships between reflectivity (Z), rain rate (R) and specific attenuation (K).

These relationships are essential, for example in the estimation of precipitation with conventional radars. In the scope of this thesis the climatological relationship between K and R is used coupled with local $Z-K$ relationships to produce locally tuned $Z-R$ relations (Section 2.6). On the other hand, the algorithm proposed in Section 2.7 for radar calibration requires precise knowledge of the climatological relationship between Z and K.

The disdrometer data used in this work come from a POSS instrument that operated on the roof of a downtown Montreal building from 1994 to 2000. The scattering model is that described by Mishchenko (2000) and the raindrop deformation model is the one proposed by Pruppacher and Beard (1970). These dataset and models were previously described in Sections 3.3 and 3.4.

5.2 Deviations from power-law

It is usually assumed that a single power-law relationship is a good approximation to the average relationships between the variables involved in radar meteorology. This idea stems from the assumption that all these variables can be interpreted as moments of a drop size distribution. Hence, the average relationships can be derived from the average DSD, for example from the Marshall-Palmer DSD.

However, the attenuation cross-section of raindrops and therefore the specific attenuation of precipitation cannot be very accurately approximated by a power-law relation. This fact was already illustrated in Fig. 2-3 and Fig. 2-4. The deviation of attenuation cross-sections from a single power-law of the raindrop diameters produces some peculiar results in the computed relationships between attenuation and the other variables.

In Fig. 5-1 and Fig. 5-2 the scatter and mean relationship between K and R and between Z and K obtained from disdrometer data in Section 3.5 are reproduced, although this time the polarization distribution of the MRO radar was used.

It is evident that a single power-law cannot fit all the values in these plots. For example, the mean $K-R$ power-law relationship over-estimates the rain rate associated with small values of attenuation. More obviously perhaps is the fact that the mean $Z-K$ power-law under-estimates the values of attenuation associated with reflectivities above $40\,dBZ$.

It is also visible how the scatter between attenuation and rain intensity in the $K-R$ plot is greater for higher intensities, while for the same range of intensities the scatter between reflectivity and attenuation in the $Z-K$ plot becomes very small.

The relationships presented in Fig. 5-1 and Fig. 5-2 were obtained by fitting the values of the variables for reflectivities higher than $20\,dBZ$. This is a good range of reflectivities for conventional radar measurements. However, as discussed before in Sections 2.5 and 4.6, dual-wavelength radars cannot measure the small attenuations produced by low reflectivities. It was also shown that we can only expect to measure attenuation values equivalent to those produced by reflectivities higher $40\,dBZ$. Therefore, in order to simulate what relationships we can expect to measure with a dual-wavelength radar we need to do the fit at higher reflectivities.

Fig. 5-3 and Fig. 5-4 show the average $K-R$ and $Z-K$ relationships found for reflectivities above $40\,dBZ$.

A striking fact emerges from these figures: the exponent in the best-fit relationship between Z and K becomes very close to one. Having a exponent so close to unity suggests that for these values of reflectivity, attenuation is almost proportional to Z.

The average $Z-R$ relationship for $Z > 40dBZ$ (not shown here) has an abnormally low exponent (1.33 compared to 1.51 for $Z > 20dBZ$). Meanwhile the exponent on the $K-R$ relationship increases from 1.18 to 1.23. These two effects combine to produce the close relationship between attenuation and reflectivity.

This puzzling behavior of X-band attenuation at higher values of reflectivity deserves a closer inspection. This finding contradicts the common perception of the radar community and has important implications that are discussed in the next section.

In addition, it should be noted that all the computations presented here were made for a temperature of 10°C. For higher values of temperature the exponent in the $Z-K$ relationship becomes even closer to one.

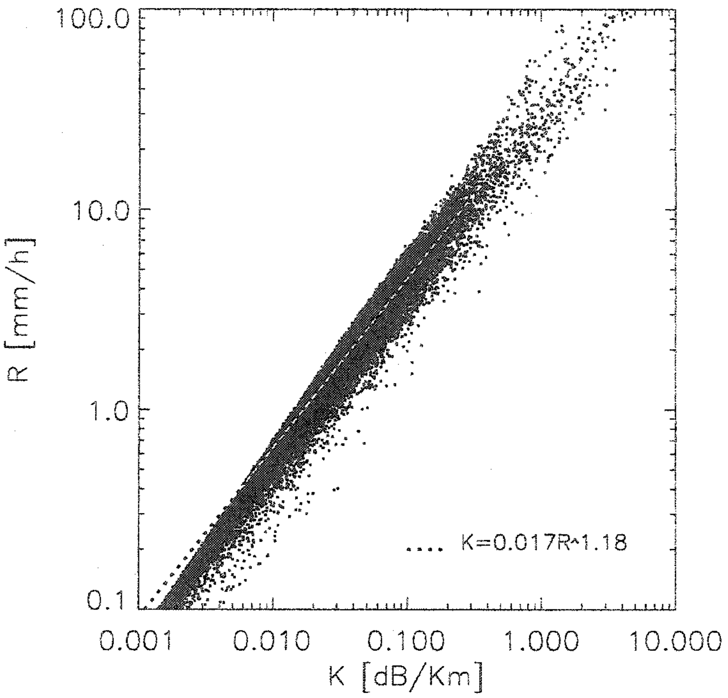

Fig. 5-1: Mean K-R relationship from McGill POSS, for Z > 20 dBZ.

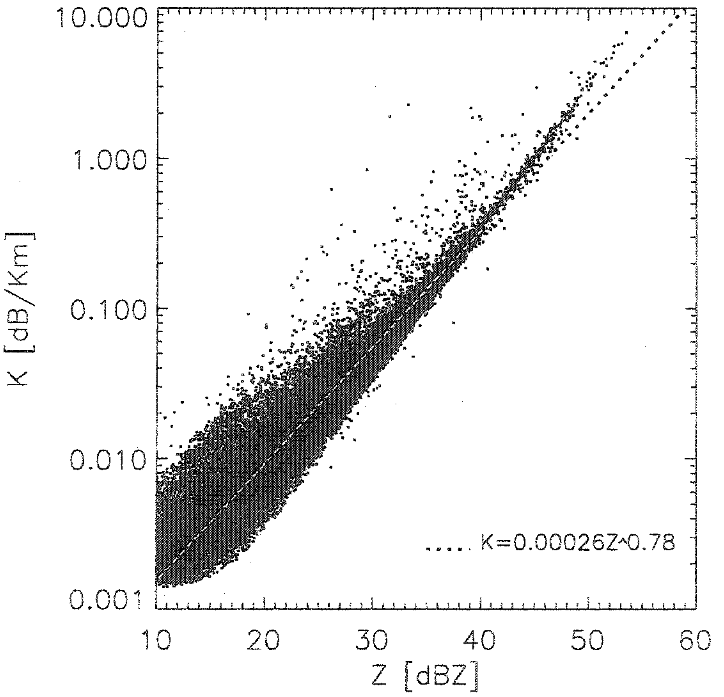

Fig. 5-2: Mean Z-K relationships from McGill POSS, for Z > 20 dBZ.

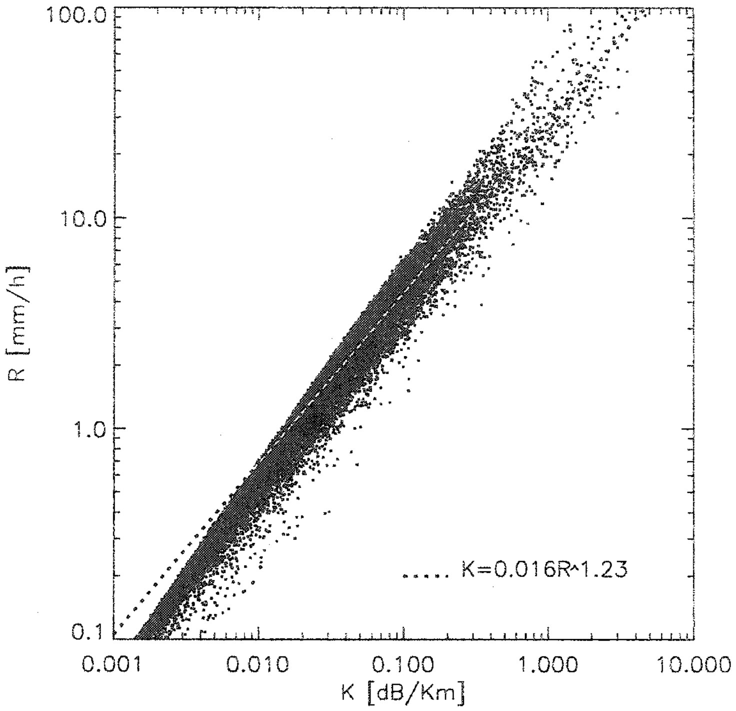

Fig. 5-3: Mean K-R relationship from McGill POSS, for Z > 40 dBZ.

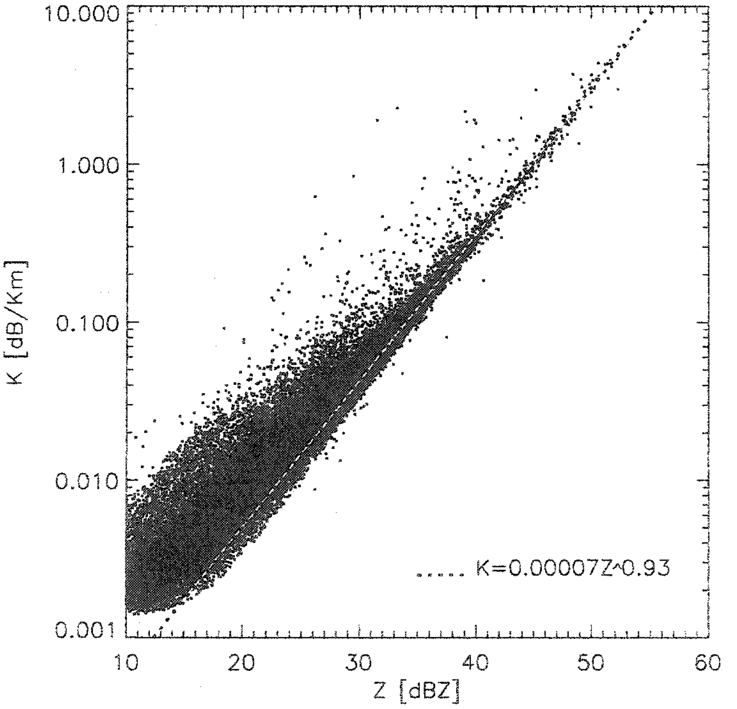

Fig. 5-4: Mean Z-K relationship from McGill POSS, for Z > 40 dBZ.

5.3 Discussion

Initially we suspected that the strange shape or our climatological $Z-K$ relationship might have been caused by problems with the attenuation cross-sections (σ_t) calculated by our scattering model.

However, after a careful examination of the model output (including cross-examination with a second scattering model) it appears that a small bulge in the attenuation cross-section produced by raindrops of diameters around $3\,mm$ is responsible for this effect (see Fig. 2-3 and Fig. 2-4).

The local slope of the relationship between σ_t and D is affected by this hump. The change in slope can be clearly appreciated in Fig. 5-5 where we repeated Fig. 2-4 with the addition of two asymptotes: one for $\sigma_t \propto D^3$ and another for $\sigma_t \propto D^6$. The asymptotes are represented by dotted lines in the plot.

The slope variation implies that while for small drops the attenuation factor ($K \propto \sum \sigma_t$) is proportional to the third power of the diameters, for larger drops ($D \sim 2mm$) it is more proportional to the sixth power of the diameters (i.e. close to reflectivity).

The attenuation cross-section dependence on the sixth power of the diameter for bigger drops explains the almost linear relationship between attenuation and reflectivity. We must remember that, as a rule of thumb, as rain intensity increases so does the concentration of big drops. Therefore, most of the reflectivity and, as we now know, also most of the attenuation is contributed by these larger drops.

Another puzzling phenomenon is that the scatter below the mean $Z-K$ line in the log-log scatter-plot between Z and K is very small. That is, it appears to be a limit for the values of the attenuation coefficient associated with each particular value of reflectivity. The limiting line is very close to our best-fit relationship for higher reflectivities. A similar effect can also be seen in the log-log scatter-plot between K and R.

It is not clear why the hump in the $\sigma_t - D$ relationship and the associated change of slope should produce a lower limit to the values of attenuation. One possible explanation is that the scatter to one side or the other of the mean $Z-K$ power-law is caused by a deficit or an excess or of big drops respectively. In the former case attenuation would not be affected significantly while the additional big drops in the latter case would contribute to attenuation in the same proportion as they contribute to reflectivity.

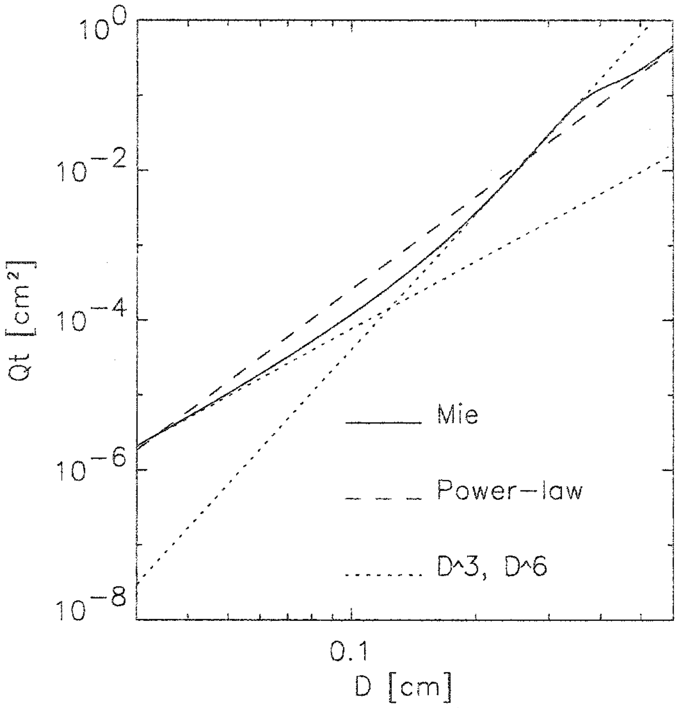

Fig. 5-5: Total attenuation cross-section of raindrops for X-band at T=10°C.

5.4 Implications

The findings in previous sections show that for reflectivities higher than around $40\,dBZ$ the X-band specific attenuation is almost proportional to reflectivity. This statement contradicts the widespread belief in the radar community [Atlas and Ulbrich, 1977; Eccles, 1979; Delrieu et al., 1991] of X-band attenuation being a good estimator of rain rate.

A troublesome fact for our dual-wavelength study is that, as previously discussed in Sections 2.5 and 4.6, it is precisely in the range of reflectivities higher than $40\,dBZ$ that dual-wavelength radars can hope to measure rain attenuation with reasonable accuracy. In particular, the algorithm proposed in Section 2.6 for locally tuning $Z-R$ relationships from attenuation measurements relies on K being almost linearly related to R. This is obviously not the case for the range of reflectivities where K can be measured.

Therefore, we have to conclude that the tuning algorithm would not work for an S- and X-band dual-wavelength radar. At least not unless the radar is capable of measuring the attenuation produced by lower reflectivities, which seems unfeasible with current technology.

Neither will any other method work that depends on measurements of X-band attenuation at high rain rates to improve upon reflectivity-only estimates. That is, for higher intensities the X-band attenuation does not add much information to that provided by reflectivity alone.

The change in slope in the relationship between reflectivity and attenuation complicates the correction of attenuation for short-wavelength single-frequency radars. Most algorithms proposed in the literature to estimate and correct for attenuation contain the assumption that attenuation is related to reflectivity by a single power-law expression [Hitschfeld and Bordan, 1953; Marzoug and Amayenc, 1991; Testud et. al., 2000].

The problems in relating attenuation to rain rate for higher rain intensities are particularly severe at X-band frequencies. This fact is aggravated by the strong temperature dependence of attenuation at these wavelengths. However, C-band radars are also affected as demonstrated by the plot in Fig. 5-6.

This situation can be important for satellite-based radars, where antenna size considerations force the use of smaller wavelengths[*]. Hence correction of attenuation is imperative. However, for wavelengths smaller than about $1\,cm$ the slope change is not very significant and attenuation can be more readily related to precipitation intensity. Fortunately, it is precisely for these frequencies where the best correlation between attenuation and rain rate is found.

In Fig. 5-7 we made use of the DSD data from the McGill POSS disdrometer to evaluate the mean error incurred in estimating rain rate from attenuation according to wavelength. The plotted data represent the root-mean-square error between the actual rain rate calculated from disdrometer data and that calculated from attenuation using the best-fit $K-R$ power-law for each frequency. Wavelengths from $1\,mm$ to $1\,m$ are displayed. The four lines represent the same results for temperatures ranging from 0°C to 30°C. The plot clearly shows a minimum error for wavelengths around 0.6 - $0.7\,cm$, which is slightly smaller that the value predicted by Atlas and Ulbrich (1974). However, attenuation measurement with dual-wavelength can be challenging due to the non-Rayleigh behavior of precipitation at these frequencies.

---

[*] The precipitation radar (PR) aboard the Tropical Rain Measurement Mission (TRMM) satellite operates at $13.8\,GHz$, $2.17\,cm$ in the Ku-band.

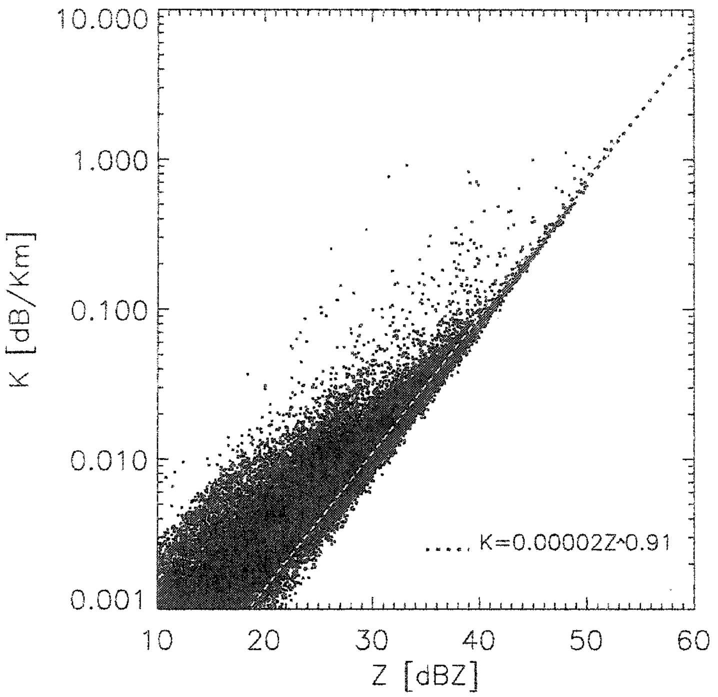

Fig. 5-6: Mean Z-K relationship at C-band for Z > 40 dBZ (from McGill POSS).

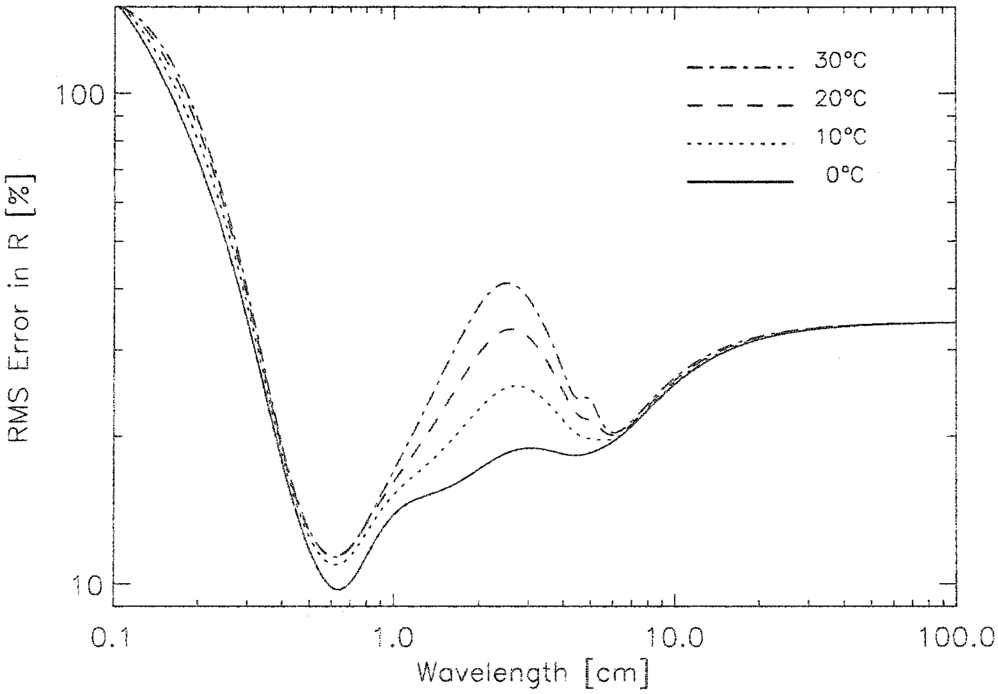

Fig. 5-7: Mean error in the estimation of rain rate from attenuation (McGill POSS data).

6 Radar calibration

6.1 Calibration algorithm

In the previous Chapter we have found that X-band attenuation is almost proportional to reflectivity for higher intensities. Despite this conclusion, another characteristic of attenuation measurements can be used to improve rainfall estimates from dual-wavelength radars.

Measured attenuation is independent of radar calibration errors. Therefore, the calibration algorithm described in Section 2.7 is not affected and the information provided by attenuation can be used for externally calibrating the radar station.

The calibration algorithm is based on the assumption that the mean $Z-K$ relationship for a time period long enough should be similar to the climatological $Z-K$ relation. Therefore, we can interpret any difference between the two relations as a radar calibration error and correct radar-measured reflectivities until they are in good agreement.

Dual-wavelength measurements of attenuation are not affected by radar calibration errors since attenuation is calculated as a difference (in units of dBZ) of a difference in reflectivities. Consequently, calibration errors are removed and only relative changes are taken into account.

6.2 Radar data

The dual-wavelength radar dataset described in Sections 4.3 and 4.4 were used to test the performance of the calibration algorithm. The dataset consists of two days (June 26 and 27, 1998) of dual-wavelength measurements by the MRO radar (Appendix C).

Two different weather systems passed over the radar in these days. On the 26th the system was moving quickly from the west, while during the 27th more local evolution took place. A radar animation of both systems can be seen at http://www.radar.mcgill.ca/~marco/thesis.html. The two systems contained cores of reflectivities in excess of 50 dBZ.

The procedure described in Section 4.6 was used in order to extract values of reflectivity and associated attenuation along 8 km-long path segments for the two days in the dataset. The reflectivity values are those measured with the S-band, so they are considered not to be affected by attenuation. The obtained scatter-plot between reflectivity and X-band specific attenuation is shown in Fig. 6-1 and Fig. 6-2 for June 26 and June 27 respectively.

The large scatter observed in the plots comes as no surprise considering the magnitude of the errors involved in the measurement of attenuation (see Section 4.2). In the case of the MRO radar the error in the estimation of S-band reflectivity was particularly severe. Since K is calculated as the difference of a difference in reflectivities, the error in the estimation of Z_S and Z_X (S-band and X-band reflectivities) appears two times each in the computation of attenuation.

The solid line in Fig. 6-1 and Fig. 6-2 corresponds to $K = 0.71\times10^{-4} Z^{0.93}$. This is the average $Z-K$ relationship obtained from the POSS data series for reflectivities above $40\,dBZ$ (Fig. 5-4). Since the employed disdrometer dataset is very long, this relationship can be regarded as a climatological relation.

In both Fig. 6-1 and Fig. 6-2 the measured values of attenuation are lower than those predicted by our climatological $Z-K$ relationship. This suggests that reflectivity was being overestimated by the MRO radar. The calibration procedure described in Section 2.7 produced the calibration errors depicted in Table 6-1.

Not surprisingly, if the plots in Fig. 6-1 and Fig. 6-2 are repeated, this time correcting reflectivity for the suggested calibration errors, a more coherent distribution of attenuation and reflectivity appears. The plots in Fig. 6-3 and Fig. 6-4 demonstrate this fact.

Day	*No. of data points*	*Ce [dB]*	*Std. Dev of Ce [dB]*
980626	*14,722*	*2.25*	*1.94*
980627	*18,306*	*1.68*	*1.95*

Table 6-1 Radar calibration errors from attenuation measurements.

6.3 Comparison with disdrometer

An external measurement of reflectivity is needed in order to assess the validity of the radar calibration errors suggested by the attenuation method presented above. Rain gauges are not appropriate in this case, not only because the inherent errors in comparing radar and rain gauges but also because our dual-wavelength data-series consists of only two days.

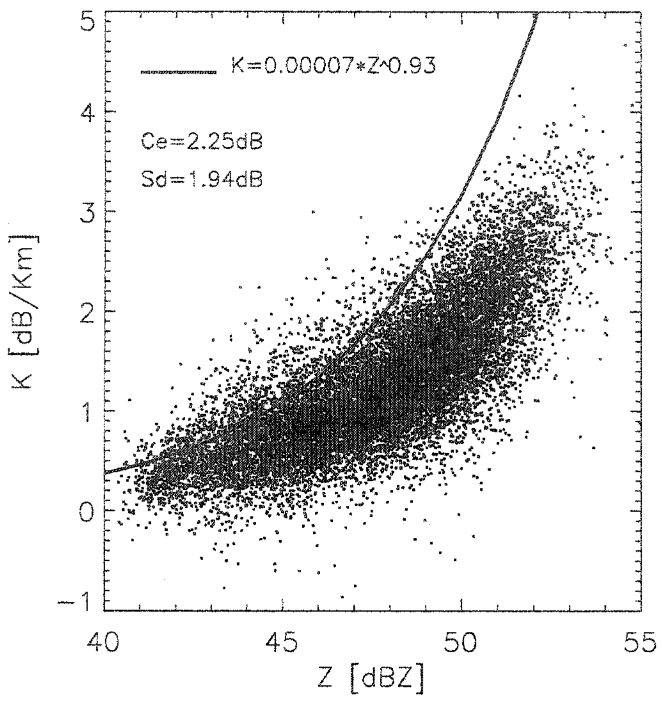

Fig. 6-1: Z-K Relationship measured for June 26, 1998.

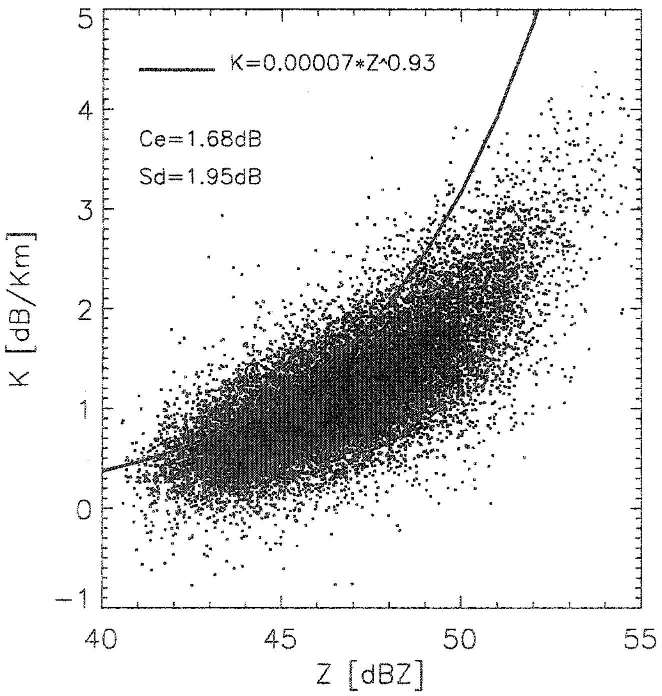

Fig. 6-2: Z-K Relationship measured for June 27, 1998.

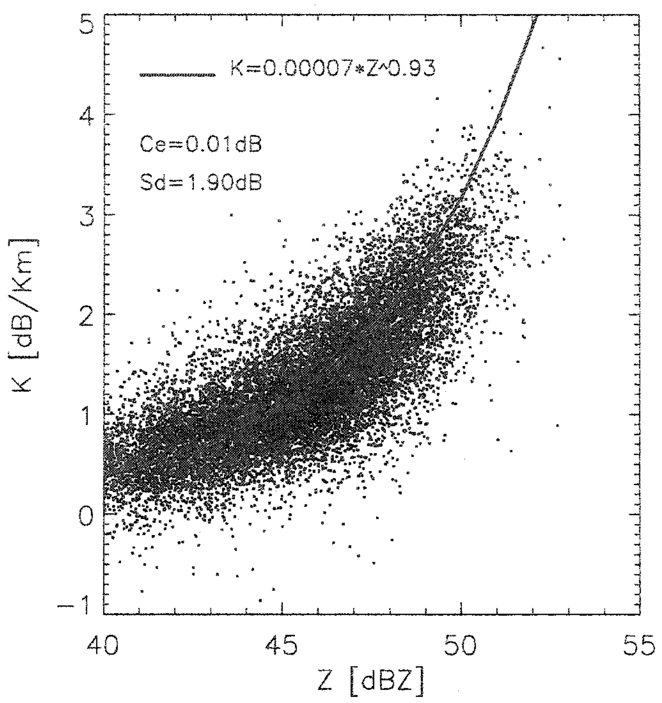

Fig. 6-3: Z-K Relationship measured for June 26, 1998, after reflectivity calibration.

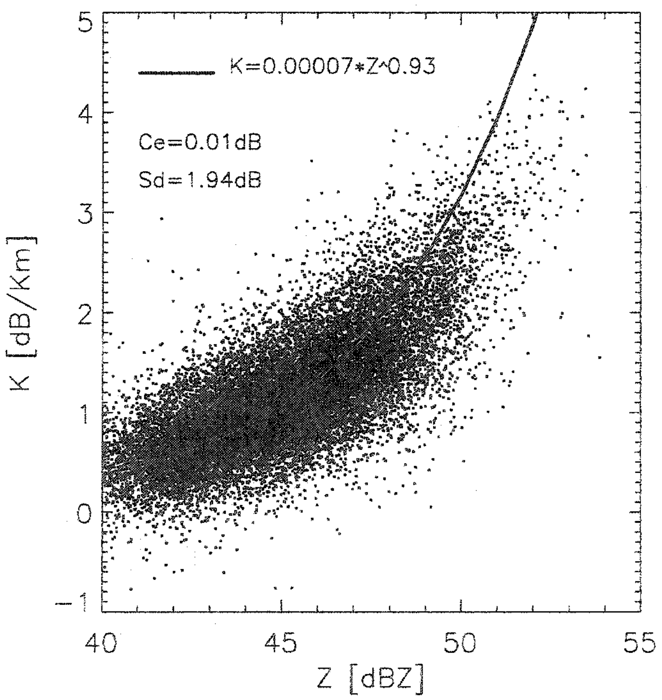

Fig. 6-4: Z-K Relationship measured for June 27, 1998, after reflectivity calibration.

Fortunately, a POSS instrument was operating about thirty kilometers away from the radar at the time of the dual-wavelength measurements. Lee and Zawadzki (2001) and Lee and Zawadzki (2002) have reported good results in using a POSS disdrometer for radar calibration.

The location of the POSS instrument on the roof of a downtown Montreal building, surrounded by other buildings and in close proximity to a small mountain*, renders the lowest elevation angles of the MRO radar unusable because they are too contaminated with ground clutter. Nevertheless, at a height of about $2\,km$ (4.1°, elevation angle No.11) the intensity of ground clutter around the POSS is sufficiently low ($\sim 9\,dB$) to permit a reasonable comparison.

Our POSS dataset for June 26 and June 27 consists of one-minute averaged drop size distributions from which reflectivity can be easily calculated. A total of 223 and 261 samples were collected for each day respectively. These data points were reduced to 190 and 225 samples after filtering out reflectivity values below the expected radar ground clutter contamination over the POSS location.

The MRO radar time resolution is five minutes. With this information and also considering the time required for precipitation to reach the ground from the height of $2\,km$, a cross-correlation between the radar and POSS reflectivities was done. Then the POSS data series was corrected by shifting the time of the samples using the best-correlated time lag.

Fig. 6-5 and Fig. 6-6 show simultaneous radar and disdrometer reflectivities for June 26 and 27, 1998. The time span is 3 hours and 10 minutes in Fig. 6-5 and 3 hours and 45 minutes in Fig. 6-6. Also included is the mean difference between the two time-series, the standard deviation and the root mean square error expressed as a percentage of POSS reflectivity.

Day	***No. of data points***	***Ce [dB]***	***Std. Dev of Ce [dB]***
980626	*190*	*2.25*	*2.69*
980627	*225*	*1.49*	*3.68*

Table 6-2 Radar calibration errors from radar-disdrometer comparison.

In both cases the measured mean difference confirms that reflectivity was overestimated by the radar. Moreover, the discrepancies between radar and POSS reflectivities agree reasonably well with the values previously estimated using the attenuation method (Table 6-1 and Table 6-2).

---

[*] Mount-Royal is approximately 234 m high.

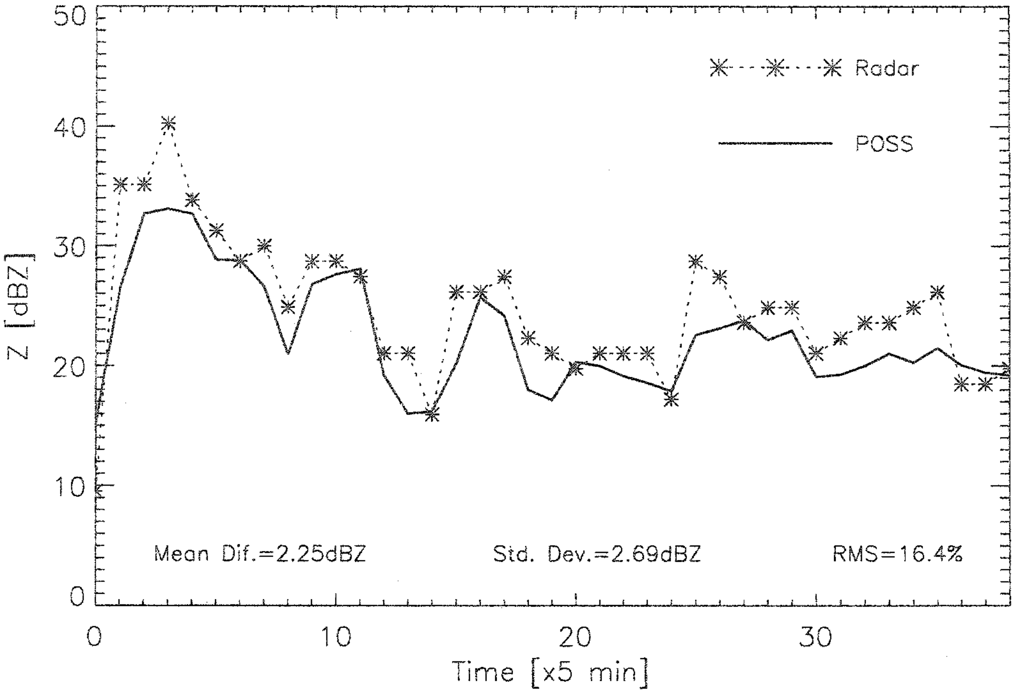

Fig. 6-5: Radar-POSS comparison for June 26, 1998.

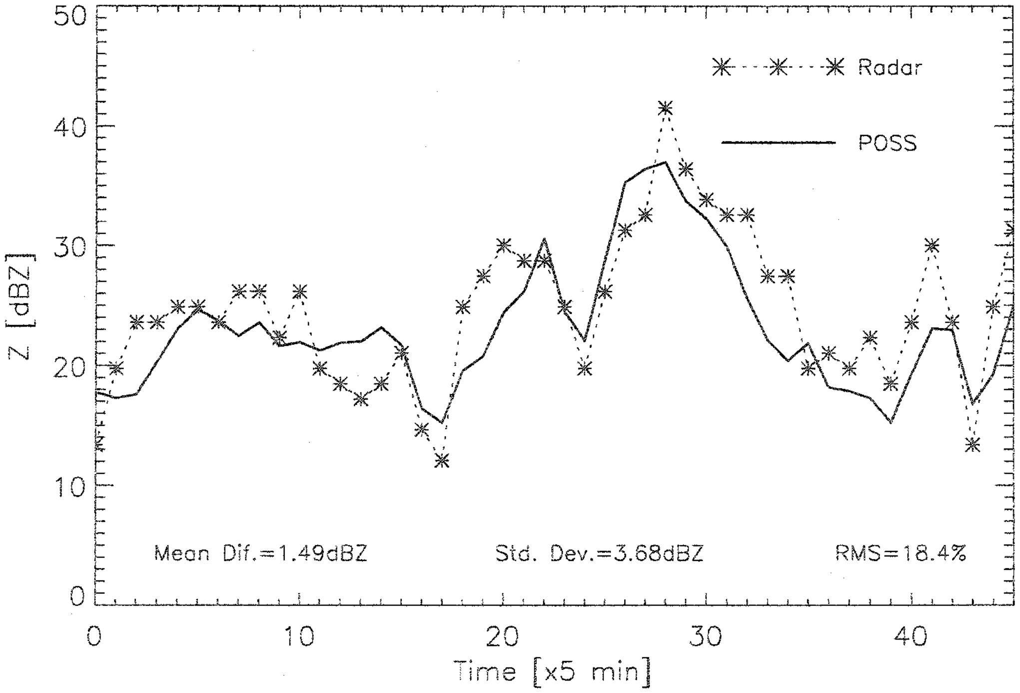

Fig. 6-6: Radar-POSS comparison for June 27, 1998.

6.4 Comments

The values of radar calibration error suggested by our dual-wavelength algorithm agree very well with the mean difference in reflectivity between the radar and an external disdrometer.

Nevertheless, our dual-wavelength data do not conclusively corroborate or refute the disdrometer-model suggestion that attenuation and reflectivity are essentially proportional for higher intensities of precipitation.

Although to the eye the climatological $Z-K$ curve fits reasonably well the data points of June 26 (Fig. 6-3), obvious disagreement exists for the highest values of reflectivity for June 27 (Fig. 6-4). In general the slope of the best power-law relationship between attenuation and reflectivity fitted to the radar data is more similar to relationships in the literature than to our disdrometer-model relations.

The average $Z-K$ relationships after reflectivity calibration for the two days in the dataset are shown in Table 6-3. These average relationships were obtained from radar data by averaging the values of attenuation in bins of reflectivity $1\,dBZ$ wide. Then, a total-fit regression was taken between the logarithm of the average attenuation ($\log\overline{K}$) and the average reflectivity values ($10\log\overline{Z}$).

A higher exponent in the $Z-K$ relationship was expected from the calculations with disdrometer data, which raises some concerns about the validity of our previous conclusions. However, our radar data is so noisy that little can be said about the accuracy of our radar-based average relationships. Further study is required to solve this apparent contradiction.

Day	***Z-K relation***
980626	$K = 0.35\times10^{-3}Z^{0.77}$
980627	$K = 0.45\times10^{-3}Z^{0.74}$

Table 6-3 Mean Z-K relationships measured by the MRO radar.

7 Conclusions

7.1 Summary

The main goal of this project is to propose a new method for improving rainfall estimates from dual-wavelength radars. We follow the rationale that the extra information provided by sensing precipitation with more than one frequency could be used to improve these estimates.

Conventional weather radars are able to estimate precipitation accumulations with an error around 40% for large areas and long time periods. Many factors affect the accuracy of radar estimates of rainfall. One of the most important issues is the uncertainty in the relationship between radar-measured reflectivity (Z) and the instantaneous rain rate (R).

This uncertainty in the $Z-R$ relationship stems from the fact that reflectivity and rain rate are mainly contributed to by different raindrop sizes. Most of the contribution to reflectivity comes from bigger drops due to the dependence of the back-scattering cross-section on the sixth power of the diameter ($Z \propto \sum D^6$). However, the main contribution to R is due to middle-size drops, because rain rate (which is equal to the summation of raindrop volume multiplied by fall velocity) is roughly proportional to the 3.67th power of the diameter ($R \propto \sum D^{3.67}$).

Therefore, the natural variability in the shape of the drop size distribution affects the relationship between reflectivity and rain rate. The problem of estimating R from Z is equivalent to the problem of estimating the concentration of middle-size drops from the concentration of bigger drops.

Our proposed method consists of finding the best-fit local relationship between reflectivity and rain attenuation (K) for a particular time period or spatial area. Then, by combining this local $Z-K$ relationship with a climatological relation between attenuation and rain rate we obtain a tuned relationship between radar-measured reflectivity and rain rate. Since attenuation is thought to be a better approximation to precipitation rate than reflectivity, by using it as a proxy for rain rate we can partially eliminate the uncertainty in the relationship between Z and R.

A simulation of this tuning algorithm was performed using two multi-year disdrometer data series divided into periods of twenty-four hours. The first dataset was collected by a POSS instrument situated in downtown Montreal while the second was gathered by an OSP disdrometer operating in Costa Rica.

Rainfall accumulations were calculated for each individual day in the data series using five different methods. First, fixed $Z-R$ and $K-R$ relationships were used, then daily $Z-R$ and daily $K-R$. Finally, our $Z-R$ tuning algorithm was tested. Each method was used to compute instantaneous rain rates from either reflectivity or attenuation. The instantaneous rates were then integrated into daily rainfall accumulations and compared to those calculated directly from disdrometer data.

The relationships employed in the single $Z-R$ and single $K-R$ methods were the best-fit relationships obtained for the whole disdrometer datasets. Therefore, the errors produced by these relations can be regarded as the minimum attainable error from either Z or K.

RMS errors were found to be around 30% for the single $Z-R$ method and 15% for the single $K-R$. However, when daily $Z-R$ relationships were used the errors decreased dramatically (RMS around 6%). Daily $Z-R$ relationships produce accumulation errors even lower than those from fixed $K-R$ relations. Nonetheless, if daily $K-R$ relationships are used (RMS around 3%) the errors decrease in the same proportion as between fixed relations. That is, K gives about half the error of Z.

Of the above methods only the one that uses a fixed $Z-R$ relation can be applied to weather radars. Daily $Z-R$ or daily $K-R$ relationships can only be found if we know R in advance. This of course is not the case with radar data. In addition, radars cannot measure attenuation with the same spatial resolution as reflectivity.

The small errors generated by daily relationships reveal that most of the DSD variability occurs in the day to day time-scale, supporting the idea of improving the estimates of precipitation through locally tuning the $Z-R$ relationship.

In our simulation, the $Z-R$ tuning algorithm was shown to produce errors similar to those generated by the use of a fixed $K-R$ relationship. This is a significant improvement over the use of a single climatological $Z-R$ relation. In addition, the tuning algorithm has the advantage of not affecting the resolution of the resulting accumulations since rain rate is estimated directly from reflectivity and maintains the same spatial and temporal resolution of the original radar measurements. It was also shown that the tuning algorithm is able to correct for radar calibration errors of reflectivity.

In spite of the pleasant properties of the tuning algorithm, a major problem concerning the feasibility of applying it to S- and X-band dual-wavelength radars was found. A close analysis of the average relationships between Z and K (from disdrometer data) revealed that for reflectivities higher than around $40\,dBZ$, the X-band specific attenuation is almost proportional to Z. This is a troublesome detail since it is precisely in this range of reflectivities where one can hope to measure attenuation with dual-wavelength radars.

Apparently, the proportionality between attenuation and reflectivity originates from the shape of the relationship between the attenuation cross-section (σ_t) of raindrops and their diameter (D). For smaller drops, σ_t is proportional to the third power of D, therefore, the summation of attenuation cross-sections is closely related to rain rate. However, for bigger drops a protuberance in the $\sigma_t(D)$ relationship causes the slope of the best-fit line (in a log-log plane) to change to a value close to six (see Fig. 5-5). Thus, for these drop diameters the summation of the attenuation cross-sections is almost proportional to reflectivity. In addition, the magnitude and location of the $\sigma_t(D)$ hump is affected by wavelength and temperature. It is particularly noticeable for higher temperatures.

The proportionality between attenuation and reflectivity has important implications for every method based on the use of X-band attenuation as a way of improving estimates of precipitation. For smaller rain intensities (where small drops dominate), attenuation is closely related to precipitation rate, while for higher rain intensities (increasing concentration of bigger drops) it becomes almost proportional to reflectivity. As a result, a single power-law relationship may not be appropriate to represent the connection between reflectivity and attenuation.

The attenuation correction algorithms for X- and C-band radars proposed in the literature assume that a single power-law relationship exists between attenuation and reflectivity. Hence, it is probably important to evaluate the impact of the more complex relationship between these two variables on the attenuation algorithms. More so, considering that most of the attenuation at X- and C-band frequencies comes precisely from higher intensities, for which the $Z-K$ proportionality is significant.

This finding can also have implications for satellite-based methods of precipitation estimation, for example: the surface reference method with TRMM to correct for reflectivity attenuation, or the direct estimation of precipitation rate from the attenuation of the affected frequencies.

Considering the problem that the $Z-K$ proportionality poses for dual-wavelength radars, as well as the characteristics of our dual-wavelength dataset (only two days of data) we decided not to attempt the tuning of the $Z-R$ relationships. Instead, another application of dual-wavelength measurements of attenuation was explored. The idea was to use radar-measured attenuation as an external way of calibrating the radar system. The underlying principle is that since attenuation is measured as a difference between reflectivities, it will not be affected by radar calibration errors.

A good radar calibration is important for the accurate measurement of rain accumulations from reflectivity. The scheme presented here is particularly appealing for Cuba where four dual-wavelength radars are in operation and no external calibration method exists.

The equations and assumptions included in the measurement of rain attenuation with dual-wavelength radars were presented, as well as a study of the error sources involved in these measurements. It was shown that with current radars employing S- and X-bands it is only possible to accurately measure attenuations of the shorter wavelength produced by reflectivities higher than around $40\,dBZ$. Smaller reflectivities produce values of attenuation too small to be detected unless very long paths are used.

In particular, our two-day MRO dataset was mainly affected by the small number of samples used in the estimation of S-band reflectivity. Also, the mismatch between the antenna beams of the two wavelengths is an important factor. This last error is reduced by the spatial integration performed in the post-detection stage of radar data processing.

The errors introduced by differential Mie scattering (two different wavelengths) and polarization (in the case of different polarizations) were also evaluated. In this regard, the MRO setup featured the worst possible choice of polarizations for each of the two frequencies. For this configuration, the differences in reflectivity between the two wavelengths produced by Mie and Z_{DR} effects add to each other. On the other hand, for the polarization configuration of the MRL-5 radars these effects oppose each other and tend to cancel each other out.

A simple procedure was described for the extraction of attenuation and reflectivity pairs. The obtained Z,K pairs were then used to calculate the mean deviation between our measured attenuation and the expected climatological value (from disdrometer and scattering model) for each reflectivity.

If the pairs of reflectivity and attenuation are extracted from a time series long enough, we can expect a climatological relationship to appear. The difference between this relationship and our measured data points can then be explained by a calibration error.

The calibration errors obtained from the above described procedure were found to compare very well with those suggested by a POSS disdrometer that was located about $30\,km$ from the MRO radar during the dual-wavelength measurements.

Nevertheless, it should be pointed out that the $Z-K$ relationships obtained from our dual-wavelength measurements (after reflectivity calibration) do not perfectly reproduce the expected climatological relation. In particular, the exponent of the measured relationships is smaller than the exponent in our climatological disdrometer-model relation. A possible cause for this apparent inconsistency might be the large scatter present in our radar measurements of attenuation.

7.2 Proposed work

Further work is required to establish solid statistics about the relationship between specific attenuation and radar reflectivity. This investigation should also shed light on the apparent discrepancy between our disdrometer-model findings and dual-wavelength radars measurements.

Disdrometer results coupled with a scattering model indicate that X-band attenuation for reflectivities higher than approximately $40\,dBZ$ do not add significant information beyond that provided by reflectivity alone. However, the $Z-K$ relationships obtained in our dual-wavelength measurements do not definitely confirm or refute this finding. More data (hopefully with better quality) is necessary to establish if there is a sustained discrepancy between theory and measurements.

We therefore recommend acquiring a robust dataset of dual-wavelength radar measurements, paying special attention to diminishing the errors in the measurement of attenuation. The MRL-5 radars in Cuba are well suited for this task.

Appendix A Characteristics of McGill POSS

Channel	*D [mm]*	*dD [mm]*	*Vt [m/s]*
1	*0.34*	*0.05*	*1.35*
2	*0.38*	*0.05*	*1.53*
3	*0.44*	*0.05*	*1.80*
4	*0.49*	*0.05*	*2.02*
5	*0.54*	*0.06*	*2.22*
6	*0.60*	*0.06*	*2.47*
7	*0.66*	*0.06*	*2.71*
8	*0.72*	*0.06*	*2.95*
9	*0.78*	*0.06*	*3.19*
10	*0.84*	*0.06*	*3.43*
11	*0.91*	*0.07*	*3.71*
12	*0.97*	*0.07*	*3.92*
13	*1.05*	*0.07*	*4.18*
14	*1.12*	*0.08*	*4.40*
15	*1.20*	*0.08*	*4.64*
16	*1.28*	*0.08*	*4.85*
17	*1.37*	*0.09*	*5.09*
18	*1.46*	*0.09*	*5.31*
19	*1.55*	*0.10*	*5.53*
20	*1.65*	*0.10*	*5.76*
21	*1.76*	*0.11*	*6.00*
22	*1.87*	*0.12*	*6.23*
23	*2.00*	*0.12*	*6.49*
24	*2.12*	*0.13*	*6.74*
25	*2.26*	*0.14*	*7.01*
26	*2.40*	*0.15*	*7.27*
27	*2.56*	*0.17*	*7.51*
28	*2.73*	*0.18*	*7.76*
29	*2.92*	*0.20*	*7.96*
30	*3.14*	*0.23*	*8.20*

31	*3.40*	*0.28*	*8.44*
32	*3.70*	*0.36*	*8.66*
33	*4.15*	*0.56*	*8.90*
34	*5.34*	*1.84*	*9.13*

Appendix B Characteristics of Costa Rica OSP

Channel	*D [mm]*	*dD [mm]*	*Vt [m/s]*
1	*0.43*	*0.11*	*1.76*
2	*0.62*	*0.24*	*2.55*
3	*0.89*	*0.28*	*3.53*
4	*1.18*	*0.30*	*4.51*
5	*1.49*	*0.31*	*5.38*
6	*1.80*	*0.31*	*6.14*
7	*2.11*	*0.31*	*6.79*
8	*2.43*	*0.31*	*7.33*
9	*2.74*	*0.32*	*7.78*
10	*3.06*	*0.32*	*8.14*
11	*3.37*	*0.32*	*8.43*
12	*3.69*	*0.32*	*8.65*
13	*4.01*	*0.32*	*8.81*
14	*4.33*	*0.32*	*8.93*
15	*4.64*	*0.32*	*9.01*
16	*4.96*	*0.32*	*9.08*

Appendix C MRO Radar

Main characteristics of the scanning radar at the J. S. Marshall Radar Observatory of McGill University as it operated during May-June, 1998:

Parameter	***S-band***	***X-band***
Transmitter type	*Klystron*	*Magnetron*
Transmitter power	*800 kW*	*75 kW*
PRF	*36 Hz (for Z)*	*520 Hz*
Antenna diameter	*9 m*	*9 m*
Beam-width	*0.86°*	*0.26°*
Antenna gain	*45 dB*	*56 dB*
Polarization	*Vertical*	*Horizontal*
Maximum range	*240/480 km*	*100 km*
Scan angles	*24 angles: 0.5° to 34.4° in two subsets of 12*	
Antenna rotation	*6 rpm*	
Volume scan time	*5 min, 2.5 min for each subset*	

Appendix D MRL-5 Radar

Main characteristics of the MRL-5 radar at the Meteorological Center of Camagüey, Cuba:

Parameter	***S-band***	***X-band***	***X-band***[*]
Transmitter type	*Magnetron*	*Magnetron*	
Trans. Power (max)	*510 (800) kW*	*160 (250) kW*	
PRF	*250/500 Hz*	*250/500 Hz*	
Antenna diameter	*4.5 m*	*1.4 m*	*4.5 m*
Beam-width	*1.5°*	*1.5°*	*0.5°*
Antenna gain	*39 dB*	*40 dB*	*49 dB*
Polarization	*Horizontal*	*Vertical*	
Maximum range	*450 km*	*450 km*	
Scan angles	*Configurable: -2.5° to 90°. Usually 10-15 angles are scanned*		
Antenna rotation	*Configurable: 0.2 to 6 rpm. Usually 4 rpm.*		
Volume scan time	*Depends on scanned angles and antenna rotation. Usually 5 min.*		

---

[*] X-band with main dish only: The antenna of the MRL-5 radar contains a small removable dish co-linearly mounted inside the antenna main dish. Both dishes are parabolic reflectors sharing their focal point. The small dish is transparent to the horizontal polarization of the S-band.

References

Andsager, K., K. V. Beard, and N. F. Laird, 1999: Laboratory measurements of axis ratios for large raindrops. *J. Atmos. Sci.*, **56**, 2673-2683.

Atlas, D., 1953: Optical extiction by rainfall. *J. Meteor.*, **10**, 486-488.

_____, and C. W. Ulbrich, 1974: The physical basis for attenuation-rainfall relationships and the measurements of rainfall parameters by combined attenuation and radar methods. *J. Rech. Atmos.*, **8**, 275-298.

_____, and _____, 1977: Path- and area-integrated rainfall measurement by microwave attenuation in the 1-3 cm band. *J. Appl. Meteor.*, **16**, 1322-1331.

Austin, P. M., 1947: Measurements of approximate raindrop size by microwave attenuation. *J. Meteor.*, **4**, 121-124.

Balanis, C. A., 1997: Antenna theory: analysis and design. *New York: Wiley*, 941p.

Battan, L. J., 1973: Radar observation of the atmosphere. *Chicago: University of Chicago Press*, 324p.

Bean, B. R., and E. J. Dutton, 1968: Radio meteorology. *Washington: U.S. Department of Commerce*, 435p.

Bringi, V. N., V. Chandrasekar, N. Balakrishnan, and D. S. Zrnic, 1990: An examination of propagation effects in rainfall on radar measurements at microwave frequencies. *J. Atmos. Sci*, **10**, 829-840.

Campos, E. F., and I. Zawadzki, 2000: Instrumental uncertainties in Z-R relations. *J. Appl. Meteor.*, **39**, 1088-1102.

Delrieu, G., J. D. Creutin, and I. Saint-Andre, 1991: Mean K-R relationships: Practical results for typical weather radar wavelengths. *J. Atmos. Oceanic Technol.*, **8**, 467-476.

Doviak, R. J., 1983: A survey of radar rain measurement techniques. *J. Climate Appl. Meteor.*, **22**, 832-849.

Eccles, P. J., 1979: Comparison of remote measurements by single- and dual-wavelength meteorological radars. *IEEE Trans. Geosci. Electron.*, **GE-17**, 205-218.

_____, and D. Atlas, 1973: A dual-wavelength radar hail detector. *J. Appl. Meteor.*, **12**, 847-854.

Fulton, R. A., J. P. Breidenbach, D. Seo, D. A. Miller, and T. O'Bannon, 1998: The WSR-88D rainfall algorithm. *Wea. Forecasting*, **13**, 377-395.

Gunn, R., and G. D. Kinzer, 1949: The terminal velocity of fall for water drops in stagnant air. *J. Meteor.*, **6**, 243-248.

Hauser, D., P. Amayenc, B. Nutten, and P. Waldteufel, 1984: A new optical instrument for simultaneous measurements of raindrop diameter and fall speed distribution. *J. Atmos. Oceanic Technol.*, **1**, 256-269.

Hitschfeld, W., and J. Bordan, 1953: Errors inherent in the radar measurements of rainfall at attenuating wavelengths. *J. Meteor.*, **11**, 58-66.

Joss, J., and A. Waldvogel, 1967: A raindrop spectrograph with automatic analysis. *Pure Appl. Geophys.*, **68**, 240-246.

Koloskov, B., B. Zimin, V. Beliaev, Y. Seregin, A. Chernikov, V. Petrov, M. Valdez, D. Martinez, C. A. Perez, and G. Puente, 1995: Results of experiments on convective precipitation enhancement in the Camaguey experimental area, Cuba. *J. App. Meteor.*, **35**, 1524-1534.

Kozu, T., and K. Nakamura, 1991: Rainfall parameter estimation from dual-radar measurements combining reflectivity profile and path-integrated attenuation. *J. Atmos. Oceanic Technol.*, **8**, 259-270.

Kummerow, C., W. Barnes, T. Kozu, J. Shiue, J. Simpson, 1998: The Tropical Rainfall Measuring Mission (TRMM) Sensor Package. *J. Atmos. Oceanic Technol.*, **15**, 809–817.

Kummerow, C., J. Simpson, O. Thiele, W. Barnes, A. T. C. Chang, E. Stocker, R. F. Adler, A. Hou, R. Kakar, F. Wentz, P. Ashcroft, T. Kozu, Y. Hong, K. Okamoto, T. Iguchi, H. Kuroiwa, E. Im, Z. Haddad, G. Huffman, B. Ferrier, W. S. Olson, E. Zipser, E. A. Smith, T. T. Wilheit, G. North, T. Krishnamurti, and K. Nakamura, 2000: The Status of the Tropical Rainfall Measuring Mission (TRMM) after Two Years in Orbit. *J. Appl. Meteor.*, **39**, 1965–1982.

Lee, G. W., and I. Zawadzki, 2001: Errors in the radar calibration by gage and disdrometer due to the variability of the drop size distribution. Preprints, *Workshop on Radar Calibration*, Albuquerque, NM, Amer. Meteor. Soc.

_____, and _____, 2002: Errors in radar measurements of precipitation due to variability of drop size distributions. Preprints, *The World Weather Research Programme's (WWRP) International*

Conference on Quantitative Precipitation Forecasting, Reading, UK, Royal Meteorological Society, **2**, 29.

Martinez, D., and E. G. Gori, 1999: Raindrop size distribution in convective clouds over Cuba. *Atmos. Res.*, **52**, 221-239.

Marshall, J. S., and W. Hitschfeld, 1953: Interpretation of the fluctuating echo from randomly distributed scatterers. Part 1. *Canadian J. Physics*, **31**, 962-994.

Marzoug, M., and P. Amayenc, 1991: Improved rain-profiling algorithm of rainfall rate with path-integrated attenuation constrain. *IEEE Trans. Geosci. Remote Sens.*, **29**, 584-592.

Melnichuk, Y. V., and Y. B. Pavlyukov, 2001: Operational adjustment of Z-R relation coefficients for radar rainfall accuracy improvement by dual-wave attenuation measurements. Preprints, *30th Conf. On Radar Meteorology*, Munich, Germany, Amer. Meteor. Soc., P16.2.

Meneghini, R., T. Kozu, H. Kumagai, and W. C. Boncyk, 1991: A study of rain estimation methods from space using dual-wavelength radar measurements at near-nadir incidence over ocean. *J. Atmos. Oceanic Technol.*, **9**, 364-382.

Mishchenko, M. I., 2000: Calculations of the amplitude matrix for a non-spherical particle in a fixed orientation. *App. Optics,* **39**, 1026-1031.

Perez, M. A., O. Rodriguez, A. Peña, R. Naranjo, L. Fernandez, A. Barreiras, A. Martinez, M. Diez, and M. Lima, 1999: Reengineering MRL-5 for the Cuban weather radar network. Preprints, *29th Radar Meteorology Conf.*, Montreal, Canada, Amer. Meteor. Soc., 14B.2, 811-812.

Pruppacher, H. R., and K. Beard, 1970: A wind tunnel investigation of the internal circulation and shape of water drops falling at terminal velocity in air. *Quart. J. Roy. Meteor. Soc.*, **96**, 247-256.

Rodriguez, O. L., M. A. Perez, R. A. Naranjo, L. L. Fernandez, A. A. Peña, and A. Barreiras, 2001: Radar data collection considerations for the Cuban weather radar network. Preprints, *30th Conf. On Radar Meteorology*, Munich, Germany, Amer. Meteor. Soc., P2.12.

Rodriguez, O. L., 1998: Optimizacion del procesamiento de las señales de video en los radares MRL-5. *Ph.D. Thesis, ISPJAE,* Havana, Cuba. 123p.

Ryzhkov, A., D. Zrnic, and D. Atlas, 1997: Polarimetrically tuned R(Z) relations and comparison of radar rainfall methods. *J. Appl. Meteor.*, **36**, 340-349.

Sachidananda, M., and D. S. Zrnic, 1986: Differential propagation phase shift and rainfall rate estimation. *Radio Sci.*, **21**(2), 235-247.

Sauvageot, H., 1992: Radar meteorology / Henri Sauvageot. *Boston: Artech House,* 366p.

Sheppard B. E., and P. I. Joe, 1993: Comparison of raindrop size distribution measurements by a Joss-Waldvogel disdrometer, a PMS 2DG spectrometer, and a POSS Doppler radar. *J. Atmos. Oceanic Technol.*, **11**, 874-887.

Sirmans, D. and R. J. Doviak, 1973: Meteorological radar signal intensity estimation. *NOAA Tech. Memo.* ERL-NSSL-64, 80p.

Smith, P. L., 1964: Interpretation of the fluctuating echo from randomly distributed scatterers: Part III. *Montreal: McGill University, Stormy Weather Group Report MW-39*, 72p.

Stout, G. E., and E. A. Mueller, 1968: Survey of relationships between rainfall rate and radar reflectivity in the measurement of precipitation. *J. Appl. Meteor.*, **7**, 465-474.

Testud, J., E. LeBouar, E. Obligis, and M. Ali-Mehenni, 2000: The rain-profiling algorithm applied to polarimetric weather radar. *J. Atmos. Oceanic Technol.*, **17**, 322-356.

Van Vleck, J. H., 1947a: Absorption of microwaves by oxigen. *Physics Rev.*, **71**, 413-424.

Van Vleck, J. H., 1947b: Absorption of microwaves by uncondensed water vapor. *Physics Rev.*, **71**, 425-433.

Woodley, W. L., A. R. Olsen, A. Hemdon, and V. Wiggert, 1975: Comparison of gage and radar methods of convective rain measurement. *J. Appl. Meteor.*, **14**, 909-928.

Zawadzki, I., 1984: Factors affecting the precision of radar measurements of rain. Preprints, *22nd Conf. On Radar Meteorology*, Zurich, Switzerland, Amer. Meteor. Soc., 251-256.